

## Numerical Solution of Non-steady Flows, Around Surfaces in Spatially and Temporally Arbitrary Motions, by using the MLPG method

R. Avila <sup>1</sup> and S. N. Atluri <sup>2</sup>

**Abstract:** The Meshless Local Petrov Galerkin (MLPG) method is used to solve the non-steady two dimensional Navier-Stokes equations. Transient laminar flow field calculations have been carried out in domains wherein certain surfaces have: (i) a sliding motion, (ii) a harmonic motion, (iii) an undulatory movement, and (iv) a contraction-expansion movement. The weak form of the governing equations has been formulated in a Cartesian coordinate system and taking into account the primitive variables of the flow field. A fully implicit pressure correction approach, which requires at each time step an iterative process to solve in a sequential manner the equations which govern the flow field, and the equations that model the corrections of pressure and velocities, has been used. The temporal discretization of the governing equations is carried out by using the Crank-Nicolson scheme. The moving Least Squares (MLS) scheme is used to generate, in a local standard domain, the shape functions of the dependent variables. The integration of the entire set of flow equations, including those equations of an elliptic elastostatic model which is used to update the position of the MLPG nodes in domains with moving surfaces, is carried out in the local standard domain by using the Gauss-Lobatto-Legendre quadrature rule. The weight function used in the MLS scheme, and in the weighted residual MLPG process, is a compactly supported fourth order spline. We conclude that the MLPG method coupled with a fully implicit pressure-correction algorithm, is a viable alternative for the solution of fluid flow problems in science and engineering, particularly those problems characterized by non-steady fluid motion around flexible bodies with undulatory or contraction-expansion movements.

**Keywords:** MLPG method, undulatory motion, non-steady fluid flow.

---

<sup>1</sup> Departamento de Termofluidos, Facultad de Ingeniería, Universidad Nacional Autónoma de México, Mexico D.F., C.P. 04510, ravila@servidor.unam.mx., Center for Aerospace Research & Education, University of California, Irvine.

<sup>2</sup> Center for Aerospace Research & Education, University of California, Irvine.

## 1 Introduction

The motion of a fluid, surrounding a natural or man-made flexible body has been, since ancient times, of great interest for human beings. Areas of interest include a wide variety of natural systems where a fluid, usually air or water, interacts with a moving body (birds or fish for example). Human beings over the centuries always wanted to emulate the flight and swimming of animals, just to fulfill their dreams or to gain advantage over their natural enemies. Since the last century the technological devices involving fluid mechanics (aerodynamics, hydrodynamics and bio-fluid dynamics), such as aerospace vehicles are continuously demanding not only the development of reliable, robust and optimal procedures to solve the mathematical models that govern the behaviour of a fluid in motion, but also the development of a full understanding of the physical phenomena involved when a flow interacts with a rigid or a flexible moving body. The proper evaluation of the flow (velocity, temperature, pressure and vorticity fields) surrounding a rigid or elastic body in motion may lead one to understand and to properly quantify, for instance, the optimal lift, drag and thrust forces governing the swimming and flight of birds, insects, micro air vehicles, and other living creatures. The understanding of the vortex structures that appear during the fluid-solid interaction in natural systems, with millions of years of evolution, can be useful, when mimicked, to increase the efficiency of engineering devices such as micro aerial vehicles (MAV) and micro-electro-mechanical systems (MEMS), etc.

Numerical calculations of the flow surrounding surfaces in arbitrary motion have often been carried out by using traditional mesh based techniques such as the finite element method, the control volume method and the spectral element method. However due to the motion of the elastic or rigid body, a time consuming remeshing must be performed in order to obtain accurate results [Sahin and Mohseni (2009)]. Due to the mesh constraints, the optimal use of the mesh based methods for the solution of problems involving moving boundaries (phase change, free-surface flows, fluid-flexible structure interactions) is still in its infancy.

Recently a novel method, the Meshless Local Petrov Galerkin (MLPG) method, has been developed. This numerical technique is characterized by the absence of a grid. The mathematical basis and the general characteristics and advantages of the MLPG method can be seen in the literature [Atluri and Zhu (1998); Lin and Atluri (2000); Lin and Atluri (2001); Atluri and Shen (2002a); Atluri and Shen (2002b); Atluri (2004); Avila and Pérez (2008); Avila and Atluri (2009)]. Among the main advantages of the MLPG method, we can mention here the following: (1) there are no mesh constraints, (2) it allows an accurate representation of complex geometrical domains, (3) the connectivity between the nodes is generated as part of the computational process and (4) the local domains surrounding each node can intersect

each other and overlap. Even though the MLPG method has been applied successfully in fields such as solid mechanics, heat transfer and fluid dynamics, it is still under development [Avila and Pérez (2008); Avila and Atluri (2009)]. In this investigation we use the MLPG method coupled with a fully implicit pressure-velocity correction approach to solve the non-steady, two dimensional Navier-Stokes equations in domains with surfaces in arbitrary spatial and temporal motions. The integration of the weak form of the governing equations (formulated in a Cartesian coordinate system) is carried out in a local domain, which is defined by the set of nodes surrounding each node located in the computational domain. The shape functions needed to approximate the flow variables in a local domain have been generated by using the Moving Least Square (MLS) scheme. To integrate the fluid equations, and to differentiate the dependent variables in systems with complex geometry, we introduce a one-to-one iso-parametric mapping between the physical and computational domains. The integration of the equations in the local domain is performed by using the Gauss-Lobatto-Legendre quadrature rule. The weight function used in the MLS scheme, as well as in the weak formulation of the equations, is a compactly supported fourth order spline. In this paper we have introduced the incompressibility constraint by using a segregated procedure. In the segregated approach the discretized continuity and momentum equations are solved sequentially. The velocities and pressure of the incompressible fluid are obtained by an iterative process that uses guessed values of the flow variables. Details of the sequential process have been published by [Avila and Pérez (2008)]. The displacement vectors of the nodes that are located in the vicinity of the moving surface are calculated by solving, using the MLPG method, an elliptic elastostatic model. The temporal discretization of the governing equations is carried out by using the Crank-Nicolson scheme [Avila and Atluri (2009)].

An outline of the paper is as follows. In Sect. 2, we present the weak form of the non-steady fluid equations, which have been defined in a local domain surrounding each MLPG node. The Crank-Nicolson scheme and the time discretization of the governing equations are given in Sect. 3. The numerical algorithm that has been used to solve the fluid equations in a sequential manner (fully implicit pressure-correction approach) is described in Sect. 4. The dynamic MLPG nodes approach (elliptic elastostatic model), which is used to compute the new position of the MLPG nodes in the flow, after a displacement step of the nodes located at the moving boundary of the solid, is presented in Sect. 5. The general aspects of the MLPG method and the MLS technique are provided in Sect. 6. In Sect. 7 we show the results for four different flow conditions with surfaces in spatially as well as temporally arbitrary motions. Finally several conclusions are drawn in Sect. 8.

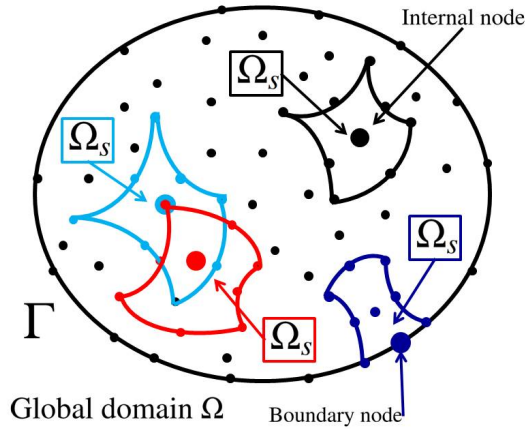


Figure 1: The scheme of the MLPG method. The global flow domain is defined as  $\Omega$  with global boundary  $\Gamma$ . The local sub-domains  $\Omega_s$ , with boundary  $\Gamma_s$ , may overlap each other.

## 2 Mathematical Models

The MLPG method is based on the solution of the weak form of the governing equations formulated over a local sub-domain  $\Omega_s$  (with boundary  $\Gamma_s$ ), which is located entirely within the global flow domain  $\Omega$  (with global boundary  $\Gamma$ ), see Fig. 1. The local sub-domain  $\Omega_s$  surrounding each MLPG node that is located, either randomly or with a certain previously known spatial distribution, in the global domain  $\Omega$ , can be of an arbitrary shape, however simple geometries like a circle or a rectangle in 2D problems, [Lin and Atluri (2000); Lin and Atluri (2001); Atluri and Shen (2002b)], or a sphere, cube or ellipsoid in 3D systems [Avila and Atluri (2009)] have been commonly used. In this paper, the local subdomain  $\Omega_s$  may have the shape of a four sided deformed region that is defined by 9 nodes, see Fig. 1. During the numerical process, the deformed 2D geometry is mapped into a quadrilateral standard local domain to perform the integration of the flow equations, see Sect. 6. The particular characteristic of the truly gridless MLPG method is that the local sub-domains may overlap each other as shown in Fig. 1. The MLPG method is based on the assumption that the union of all local sub-domains  $\Omega_s$  represents the entire flow domain  $\Omega$  in such a manner that  $\cup \Omega_s \supset \Omega$ . Consequently as long as the union of all local sub-domains  $\Omega_s$  covers the entire flow domain  $\Omega$ , the global

weak form of the governing equations and the boundary conditions, will be satisfied *a posteriori* in the global domain  $\Omega$  and on the boundary  $\Gamma$ , respectively [Lin and Atluri (2000); Lin and Atluri (2001); Atluri and Shen (2002b)]. In the local weak formulation of the non-steady, incompressible fluid flow equations, we assume that the test function  $w$  [as in the continuity equation (1)] or each of the test functions  $w_i$  [as in the momentum equations (2)] over each local sub-domain  $\Omega_s$ , are the same as the weight function used to digitally generate the trial functions of the dependent flow variables (Moving Least Squares (MLS) numerical technique, see Sect. 6). This way to select the test function over  $\Omega_s$  has been called by Atluri and Shen (2002b) as the MLPG1 approach. The analytical expression of the scalar weight function  $w$  (or each of the  $w_i$ ) that we use, correspond to a fourth order function of compact support. Additionally it should be mentioned, that we use the same scalar fourth order test function  $w$ , to obtain the weak form of each of the following equations that we have solved in this investigation: (i) continuity equation, (ii)  $x_1$  and  $x_2$  momentum equations, (iii) energy equation, (iv) fully implicit approach equations, and (v) the elliptic elastostatic model equations. In the MLPG method, the trial functions generated by a computational procedure and the test functions (usually selected as analytical expressions) over each of the local sub-domains  $\Omega_s$ , belong to different spaces. Therefore the weak form of the governing equations in the local sub-domain  $\Omega_s$  is written as follows

#### Continuity Equation

$$- \int_{\Omega_s} (\rho \mathbf{v} \cdot \nabla w) d\Omega + \int_{\Gamma_s} (\rho \mathbf{v} \cdot \vec{\eta} w) d\Gamma = 0, \quad (1)$$

where  $\rho$  and  $\mathbf{v}$  are the density and the velocity vector of the fluid respectively,  $w$  is a test function (a scalar analytical expression),  $\vec{\eta}$  is an outward unit vector, and  $\Omega_s$  and  $\Gamma_s$  are the volume and the surface of the local flow domain surrounding each of the MLPG nodes respectively.

#### Momentum Equation

$$\begin{aligned}
 \int_{\Omega_s} \rho \frac{\partial \mathbf{v}}{\partial t} \cdot \mathbf{w} d\Omega + \int_{\Omega_s} \rho \mathbf{v} \cdot \nabla \mathbf{v} \cdot \mathbf{w} d\Omega - \int_{\Omega_s} \rho \mathbf{g} \cdot \mathbf{w} d\Omega - \int_{\Omega_s} p \nabla \cdot \mathbf{w} d\Omega + \\
 \int_{\Omega_s} \boldsymbol{\tau} \cdot \nabla \cdot \mathbf{w} d\Omega + \int_{\Gamma_s} p \vec{\eta} \cdot \mathbf{w} d\Gamma - \int_{\Gamma_s} \boldsymbol{\tau} \cdot \vec{\eta} \cdot \mathbf{w} d\Gamma = 0, \quad (2)
 \end{aligned}$$

where  $\mathbf{w}$  is a test function vector ( $\mathbf{w} = w_i \mathbf{i}_i$ ),  $p$  is the pressure,  $\mathbf{g}$  is the gravity vector,  $\boldsymbol{\tau}$  is the viscous stress tensor, which is defined by

$$\tau_{ij} = \mu \left( \frac{\partial v_i}{\partial x_j} + \frac{\partial v_j}{\partial x_i} \right), \quad (3)$$

and  $\mu$  is the dynamic viscosity of the fluid. Eq. (2) can also be written as [Lin and Atluri (2001); Foias, Manley, Rosa, and Temam (2001); Atluri and Shen (2002a); Atluri (2004)]

$$\begin{aligned} \int_{\Omega_s} \rho \frac{\partial v_j}{\partial t} w_j d\Omega + \int_{\Omega_s} \rho v_i \frac{\partial v_j}{\partial x_i} w_j d\Omega - \int_{\Omega_s} \rho g_j w_j d\Omega - \int_{\Omega_s} p \frac{\partial w_j}{\partial x_j} d\Omega + \\ \int_{\Omega_s} \tau_{ji} \frac{\partial w_j}{\partial x_i} d\Omega + \int_{\Gamma_s} p n_j w_j d\Gamma - \int_{\Gamma_s} \tau_{ji} \eta_i w_j d\Gamma = 0. \end{aligned} \quad (4)$$

Taking into account the expression of the viscous stress tensor, Eq. (3), and by assuming in the test function vector  $\mathbf{w}$  that  $w_1 = w_2 = w_3 = w$ , Eq. (4), along the  $\mathbf{i}_j$  direction, can be written as

$$\begin{aligned} \int_{\Omega_s} \rho \frac{\partial v_j}{\partial t} w d\Omega + \int_{\Omega_s} \rho v_i \frac{\partial v_j}{\partial x_i} w d\Omega - \int_{\Omega_s} \rho g_j w d\Omega - \int_{\Omega_s} p \frac{\partial w}{\partial x_j} d\Omega + \\ \int_{\Omega_s} \mu \frac{\partial v_j}{\partial x_i} \frac{\partial w}{\partial x_i} d\Omega + \int_{\Omega_s} \mu \frac{\partial v_i}{\partial x_j} \frac{\partial w}{\partial x_i} d\Omega + \int_{\Gamma_s} p n_j w d\Gamma - \int_{\Gamma_s} \mu \frac{\partial v_j}{\partial x_i} \eta_i w d\Gamma - \\ \int_{\Gamma_s} \mu \frac{\partial v_i}{\partial x_j} \eta_i w d\Gamma = 0. \end{aligned} \quad (5)$$

### Energy Equation

$$\begin{aligned} \int_{\Omega_s} \frac{\partial T}{\partial t} w d\Omega + \int_{\Omega_s} \mathbf{v} \cdot \nabla T w d\Omega + \int_{\Omega_s} \alpha \nabla T \cdot \nabla w d\Omega - \int_{\Gamma_s} \alpha \nabla T \cdot \vec{\eta} w d\Gamma - \\ \int_{\Omega_s} \frac{S_E}{\rho C_p} w d\Omega = 0, \end{aligned} \quad (6)$$

where  $T$  is the temperature,  $\alpha$  is the thermal diffusivity,  $C_p$  is the specific heat and  $S_E$  is a source of thermal energy (rate of thermal energy generation per unit volume). Note that the same test function  $w$  has been used in the weak form of Eqs. (1), (5) and (6).

### 3 Time discretization

The temporal term of the non-steady fluid flow equations (see Eqs. (5) and (6)) has been discretized by using the Crank-Nicolson scheme which is the average of the forward Euler method (dependent variables evaluated at the time step  $n$ , explicit approach) and the backward Euler method (dependent variables evaluated at the time step  $n + 1$ , implicit approach). If we add the explicit and implicit expressions,

with the time derivative approximated by

$$\frac{\partial v_j}{\partial t} = \frac{v_j^{(n+1)} - v_j^n}{\Delta t} \quad \text{and} \quad \frac{\partial T}{\partial t} = \frac{T^{(n+1)} - T^n}{\Delta t}, \quad (7)$$

we obtain the following expressions:

*Momentum equation*

$$\begin{aligned} & 2 \int_{\Omega_s} \frac{\rho v_j^{n+1}}{\Delta t} w d\Omega + \int_{\Omega_s} \rho v_i^{(n+1)} \frac{\partial v_j^{(n+1)}}{\partial x_i} w d\Omega - \int_{\Omega_s} \rho g_j^{(n+1)} w d\Omega - \\ & \int_{\Omega_s} p^{(n+1)} \frac{\partial w}{\partial x_j} d\Omega + \int_{\Omega_s} \mu \frac{\partial v_j^{(n+1)}}{\partial x_i} \frac{\partial w}{\partial x_i} d\Omega + \int_{\Omega_s} \mu \frac{\partial v_i^{(n+1)}}{\partial x_j} \frac{\partial w}{\partial x_i} d\Omega + \\ & \int_{\Gamma_s} p^{(n+1)} n_j w d\Gamma - \int_{\Gamma_s} \mu \frac{\partial v_j^{(n+1)}}{\partial x_i} \eta_i w d\Gamma - \int_{\Gamma_s} \mu \frac{\partial v_i^{(n+1)}}{\partial x_j} \eta_i w d\Gamma = \\ & 2 \int_{\Omega_s} \frac{\rho v_j^n}{\Delta t} w d\Omega - \int_{\Omega_s} \rho v_i^n \frac{\partial v_j^n}{\partial x_i} w d\Omega + \int_{\Omega_s} \rho g_j^n w d\Omega + \\ & \int_{\Omega_s} p^n \frac{\partial w}{\partial x_j} d\Omega - \int_{\Omega_s} \mu \frac{\partial v_j^n}{\partial x_i} \frac{\partial w}{\partial x_i} d\Omega - \int_{\Omega_s} \mu \frac{\partial v_i^n}{\partial x_j} \frac{\partial w}{\partial x_i} d\Omega - \\ & \int_{\Gamma_s} p^n n_j w d\Gamma + \int_{\Gamma_s} \mu \frac{\partial v_j^n}{\partial x_i} \eta_i w d\Gamma + \int_{\Gamma_s} \mu \frac{\partial v_i^n}{\partial x_j} \eta_i w d\Gamma. \end{aligned} \quad (8)$$

*Energy equation*

$$\begin{aligned} & 2 \int_{\Omega_s} \frac{T^{(n+1)}}{\Delta t} w d\Omega + \int_{\Omega_s} v_i^{(n+1)} \frac{\partial T^{(n+1)}}{\partial x_i} w d\Omega + \int_{\Omega_s} \alpha \frac{\partial T^{(n+1)}}{\partial x_i} \frac{\partial w}{\partial x_i} - \\ & \int_{\Gamma_s} \alpha \frac{\partial T^{(n+1)}}{\partial x_i} \eta_i w d\Gamma - \int_{\Omega_s} \frac{S_E^{(n+1)}}{\rho C_P} w d\Omega = \\ & 2 \int_{\Omega_s} \frac{T^n}{\Delta t} w d\Omega - \int_{\Omega_s} v_i^n \frac{\partial T^n}{\partial x_i} w d\Omega - \int_{\Omega_s} \alpha \frac{\partial T^n}{\partial x_i} \frac{\partial w}{\partial x_i} + \\ & \int_{\Gamma_s} \alpha \frac{\partial T^n}{\partial x_i} \eta_i w d\Gamma + \int_{\Omega_s} \frac{S_E^n}{\rho C_P} w d\Omega. \end{aligned} \quad (9)$$

#### 4 A fully implicit pressure-velocity correction approach to solve the fluid equations

Due to the non-linear nature of the momentum equation, a segregated solution algorithm has been used to solve Eqs. (1) and (8) in a sequential manner. To obtain

a converged solution of the governing equations at each time step  $n + 1$ , from the velocity and pressure fields known at the previous time step  $n$ , we use the following iterative fully implicit pressure-velocity correction approach:

1).-From the values of  $v_j$  and  $p$ , known at the previous time step  $n$  (a particular case is when  $n = 0$ , i.e. at  $t = 0$ ), we propose to use these known values as the guessed values for the velocities  $v_j^{*(n+1)}$  and pressure  $p^{*(n+1)}$  to be used in the solution of the  $x_1$  ( $j = 1$ ) momentum equation, see Eq. (8). Note that the guessed value  $v_1^{*(n+1)}$  is only used in the convective term

$$\int_{\Omega_s} \rho v_1^{*(n+1)} \frac{\partial v_1^{(n+1)}}{\partial x_1} w d\Omega, \quad (10)$$

whereas in the rest of the terms of Eq. (8), the guessed values for  $v_2^{*(n+1)}$ ,  $v_3^{*(n+1)}$  and  $p^{*(n+1)}$  are used in such a manner that the only unknown variable is  $v_1^{(n+1)}$ . Hence we first solve the  $x_1$  momentum equation.

2).-Now we have an updated value for the  $v_1^{(n+1)}$  velocity, in the segregated algorithms it is usually written as  $v_1^{**(n+1)}$ . The updated velocity  $v_1^{**(n+1)}$  and the guessed values for  $v_2^{*(n+1)}$ ,  $v_3^{*(n+1)}$  and  $p^{*(n+1)}$  are now used to solve the  $x_2$  ( $j = 2$ ) momentum equation, see Eq. (8), in such a manner that the only unknown variable is  $v_2^{(n+1)}$ .

3).-Now we have an updated value for the  $v_2^{(n+1)}$  velocity, i.e.  $v_2^{**(n+1)}$ . If the problem is three-dimensional, the updated velocities  $v_1^{**(n+1)}$  and  $v_2^{**(n+1)}$ , and the guessed values for  $v_3^{*(n+1)}$  and  $p^{*(n+1)}$  are now used to solve the  $x_3$  ( $j = 3$ ) momentum equation, see Eq. (8), in such a manner that the only unknown variable is  $v_3^{(n+1)}$ .

4).-Now we have also an updated value for the  $v_3^{(n+1)}$  velocity, i.e.  $v_3^{**(n+1)}$ .

5).-The three updated velocities  $v_1^{**(n+1)}$ ,  $v_2^{**(n+1)}$  and  $v_3^{**(n+1)}$  are used in the continuity equation Eq. (1), to obtain a residual of mass  $\Delta \dot{m}$ , i.e.

$$-\int_{\Omega_s} \rho v_i^{**(n+1)} \frac{\partial w}{\partial x_i} d\Omega + \int_{\Gamma_s} \rho v_i^{**(n+1)} \eta_i w d\Gamma = \Delta \dot{m}. \quad (11)$$

6).-The correction of velocities  $v'_j$  and pressure  $p'$  are defined by the following expressions:

$$v_j^{n+1} = v_j^{**(n+1)} + v'_j \quad \text{and} \quad p^{n+1} = p^{*(n+1)} + p', \quad (12)$$

if we assume that Eqs. (12) exactly satisfy the continuity equation, Eq. (1), we may write:

$$-\int_{\Omega_s} \rho v_i^{**(n+1)} \frac{\partial w}{\partial x_i} d\Omega - \int_{\Omega_s} \rho v'_i \frac{\partial w}{\partial x_i} d\Omega + \int_{\Gamma_s} \rho v_i^{**(n+1)} \eta_i w d\Gamma + \int_{\Gamma_s} \rho v'_i \eta_i w d\Gamma = 0.$$

(13)

Subtracting Eq. (13) from Eq. (11) we obtain the first equation for the correction of velocities:

$$\int_{\Omega_s} \rho v'_i \frac{\partial w}{\partial x_i} d\Omega - \int_{\Gamma_s} \rho v'_i \eta_i w d\Gamma = \Delta \dot{m}. \quad (14)$$

7).-We substitute the previously calculated velocity  $v_1^{**(n+1)}$  into the  $j = 1$  momentum equation, Eq. (8), hence we have

$$\begin{aligned} & 2 \int_{\Omega_s} \rho \frac{v_1^{**(n+1)}}{\Delta t} w d\Omega + \int_{\Omega_s} \rho v_i^{*(n+1)} \frac{\partial v_1^{**(n+1)}}{\partial x_i} w d\Omega - \int_{\Omega_s} \rho g_1^{(n+1)} w d\Omega - \\ & \int_{\Omega_s} p^{*(n+1)} \frac{\partial w}{\partial x_1} d\Omega + \int_{\Omega_s} \mu \frac{\partial v_1^{**(n+1)}}{\partial x_i} \frac{\partial w}{\partial x_i} d\Omega + \int_{\Omega_s} \mu \frac{\partial v_1^{**(n+1)}}{\partial x_1} \frac{\partial w}{\partial x_1} d\Omega + \\ & \int_{\Omega_s} \mu \frac{\partial v_2^{*(n+1)}}{\partial x_1} \frac{\partial w}{\partial x_2} d\Omega + \int_{\Omega_s} \mu \frac{\partial v_3^{*(n+1)}}{\partial x_1} \frac{\partial w}{\partial x_3} d\Omega - \int_{\Gamma_s} \mu \frac{\partial v_1^{**(n+1)}}{\partial x_i} \eta_i w d\Gamma - \\ & \int_{\Gamma_s} \mu \frac{\partial v_1^{**(n+1)}}{\partial x_1} \eta_1 w d\Gamma - \int_{\Gamma_s} \mu \frac{\partial v_2^{*(n+1)}}{\partial x_1} \eta_2 w d\Gamma - \int_{\Gamma_s} \mu \frac{\partial v_3^{*(n+1)}}{\partial x_1} \eta_3 w d\Gamma + \\ & \int_{\Gamma_s} p^{*(n+1)} \eta_1 w d\Gamma = \text{RHS}, \end{aligned} \quad (15)$$

where RHS is the right hand side term of Eq. (8) which corresponds to the known values at the  $n$  time step. Now we assume that Eqs. (12) also satisfy the  $j = 1$  momentum equation, see Eq. (8), therefore by substituting  $v_1^{n+1} = v_1^{**(n+1)} + v'_1$  and  $p^{n+1} = p^{*(n+1)} + p'$  into Eq. (8) we generate another momentum equation along  $x_1$  direction that involves the correction of velocity  $v'_1$  and the correction of pressure  $p'$ . By subtracting this new equation (whose right hand side is also RHS) from Eq. (15), we obtain a second equation that takes into account the correction of the velocity  $v'_1$  and the correction of pressure  $p'$ , hence we have:

$$\begin{aligned} & -2 \int_{\Omega_s} \rho \frac{v'_1}{\Delta t} w d\Omega - \int_{\Omega_s} \rho v_i^{*(n+1)} \frac{\partial v'_1}{\partial x_i} w d\Omega + \int_{\Omega_s} p' \frac{\partial w}{\partial x_1} d\Omega - \int_{\Omega_s} \mu \frac{\partial v'_1}{\partial x_i} \frac{\partial w}{\partial x_i} d\Omega - \\ & \int_{\Omega_s} \mu \frac{\partial v'_1}{\partial x_1} \frac{\partial w}{\partial x_1} d\Omega + \int_{\Gamma_s} \mu \frac{\partial v'_1}{\partial x_i} \eta_i w d\Gamma + \int_{\Gamma_s} \mu \frac{\partial v'_1}{\partial x_1} \eta_1 w d\Gamma - \int_{\Gamma_s} p' \eta_1 w d\Gamma = 0. \end{aligned} \quad (16)$$

A similar procedure can be carried out to obtain, from the momentum equation along the other two directions  $x_2$  ( $j = 2$ ) and  $x_3$  ( $j = 3$ ), the equations for the correction of velocities  $v'_2$  and  $v'_3$  and pressure  $p'$ .

8).-The third equation that includes the correction of the velocity  $v'_2$  and the correction of pressure  $p'$  is the following:

$$\begin{aligned}
 & -2 \int_{\Omega_s} \rho \frac{v'_2}{\Delta t} w d\Omega - \int_{\Omega_s} \rho v_1^{*(n+1)} \frac{\partial v'_2}{\partial x_1} w d\Omega - \int_{\Omega_s} \rho v_2^{*(n+1)} \frac{\partial v'_2}{\partial x_2} w d\Omega - \\
 & \int_{\Omega_s} \rho v_3^{*(n+1)} \frac{\partial v'_2}{\partial x_3} w d\Omega + \int_{\Omega_s} p' \frac{\partial w}{\partial x_2} d\Omega - \int_{\Omega_s} \mu \frac{\partial v'_2}{\partial x_i} \frac{\partial w}{\partial x_i} d\Omega - \\
 & \int_{\Omega_s} \mu \frac{\partial v'_2}{\partial x_2} \frac{\partial w}{\partial x_2} d\Omega + \int_{\Gamma_s} \mu \frac{\partial v'_2}{\partial x_i} \eta_i w d\Gamma + \int_{\Gamma_s} \mu \frac{\partial v'_2}{\partial x_2} \eta_2 w d\Gamma - \\
 & \int_{\Gamma_s} p' \eta_2 w d\Gamma = 0.
 \end{aligned} \tag{17}$$

9).-The fourth equation that involves the correction of the velocity  $v'_3$  and the correction of pressure  $p'$  is written as

$$\begin{aligned}
 & -2 \int_{\Omega_s} \rho \frac{v'_3}{\Delta t} w d\Omega - \int_{\Omega_s} \rho v_1^{*(n+1)} \frac{\partial v'_3}{\partial x_1} w d\Omega - \int_{\Omega_s} \rho v_2^{*(n+1)} \frac{\partial v'_3}{\partial x_2} w d\Omega - \\
 & \int_{\Omega_s} \rho v_3^{*(n+1)} \frac{\partial v'_3}{\partial x_3} w d\Omega + \int_{\Omega_s} p' \frac{\partial w}{\partial x_3} d\Omega - \int_{\Omega_s} \mu \frac{\partial v'_3}{\partial x_i} \frac{\partial w}{\partial x_i} d\Omega - \\
 & \int_{\Omega_s} \mu \frac{\partial v'_3}{\partial x_3} \frac{\partial w}{\partial x_3} d\Omega + \int_{\Gamma_s} \mu \frac{\partial v'_3}{\partial x_i} \eta_i w d\Gamma + \int_{\Gamma_s} \mu \frac{\partial v'_3}{\partial x_3} \eta_3 w d\Gamma - \\
 & \int_{\Gamma_s} p' \eta_3 w d\Gamma = 0.
 \end{aligned} \tag{18}$$

Notice that the four equations, Eqs. (14), (16), (17) and (18) constitute a system of four equations with four unknown variables ( $v'_1$ ,  $v'_2$ ,  $v'_3$  and  $p'$ ).

10).-After the solution of the system of equations, we proceed to obtain an updated value for the variables at the  $n + 1$  time step as

$$v_j^{n+1} = v_j^{*(n+1)} + \gamma_j v'_j \quad \text{and} \quad p^{n+1} = p^{*(n+1)} + \gamma_p p', \tag{19}$$

where  $\gamma_j$  and  $\gamma_p$  are under-relaxation parameters which act to slow down the changes, from iteration to iteration, in the value of the updated variables. The particular value of the  $\gamma$  under-relaxation parameters depends on the case under study, however it is in the range  $0 < \gamma < 1$ . The updated values are then taken as the guessed values for the next iteration, hence we have

$$v_j^{*(n+1)} = v_j^{n+1} \quad \text{and} \quad p^{*(n+1)} = p^{n+1}. \tag{20}$$

11).-If the system includes buoyancy due to the gravity force and temperature gradients, the energy equation, Eq. (9), is solved.

12).-Verify convergence. If the convergence criterion is not satisfied go to step 1 and initiate the process to calculate another set of corrections for velocity and pressure. On the other hand, if the convergent criterion is satisfied, we increase the time (by  $\Delta t$ ) and go to step 1 to initiate the iterative process to get convergence for the next time step.

## 5 An Arbitrary Lagrangian Eulerian (ALE) formulation and an elliptic elastostatic model for the repositioning of the MLPG nodes, due to a Solid Surface in Motion in the Fluid Domain

During the last three decades, fluid-solid interaction, and free-surface problems have been traditionally solved by using mesh based numerical algorithms, which have been coupled with an interface-tracking (moving-mesh) method known as the Arbitrary Lagrangian-Eulerian (ALE) formulation [Hughes, Liu, and Zimmermann (1981); Donea, Giuliani, and Halleux (1982)]. In the ALE kinematical description of the flow domain, the grid points (in our case the MLPG nodes) are displaced independently of the fluid motion. In the moving mesh based methods, as the solid body moves and the spatial flow domain changes its shape, the mesh moves to follow ("track") the fluid-solid body interface. Tracking the interface by moving the fluid mesh allows one to control the mesh resolution in critical regions with large velocity or temperature gradients, and to obtain better results in problems with complex geometry.

In this investigation we compute the transient flow field in systems wherein *certain boundaries (or surfaces) are moving with a prescribed law of motion*. Hence as time elapses, we know that at the time steps  $n$  and  $n + 1$ , the position vectors of the MLPG nodes located at the moving solid boundary are  $\mathbf{X}^n$  and  $\mathbf{X}^{n+1}$  respectively (consequently we know the displacement vector  $\mathbf{u}_b = \mathbf{X}^{n+1} - \mathbf{X}^n$ ). We assume that the displacement  $\mathbf{u}_b$  of each of the MLPG nodes located at the fluid-solid interface, influences the displacement  $\mathbf{u}$  of the MLPG nodes located elsewhere in the flow domain, in the vicinity of the moving surfaces. We use a Quasi-Eulerian approach (QE), in which the MLPG nodes move continuously with the motion of the moving boundary, in such a manner that the position of any MLPG node in the flow domain is only a function of the prescribed law of motion of the nodes located at the moving boundary. Therefore the motion of the nodes located in the flow domain, induced by the moving surfaces, is independent of the velocity of the fluid at this node. As we deal with the motion of the MLPG nodes, we should also deal with the velocity of the MLPG nodes. The Quasi-Eulerian approach makes the assumption that the velocity  $\hat{\mathbf{v}}$  of the MLPG nodes located in the flow domain is small in magnitude compared to the velocity of the fluid  $\mathbf{v}$  [Gwynllyw and Phillips (2005)]. If  $\hat{\mathbf{v}} \approx 0$ , the ALE formulation leads to an Eulerian approach in which the so called convective

velocity  $\mathbf{c}$  is simply identical to the velocity of the fluid  $\mathbf{v}$ . Hence the local time derivative of the  $v_j$  fluid velocity in the referential domain (defined by the MLPG nodes)  $\Omega_{\hat{\mathbf{x}}}$  is approximated by, see Eq. (7) [Donea, Huerta, Ponthot, and Rodríguez-Ferran (2005); Gwynllyw and Phillips (2005)]

$$\left. \frac{\partial v_j}{\partial t} \right|_{\hat{\mathbf{x}}} \approx \frac{v_j^{(n+1)} - v_j^n}{\Delta t}, \quad (21)$$

where  $v_j^{(n+1)}$  and  $v_j^n$  are the fluid velocities evaluated at the same moving MLPG node at consecutive time steps. Regarding the velocity of the nodes located at the moving boundary, we assume locally a purely Lagrangian approach, which implies that the velocity of the fluid in contact with the boundary is the same as the velocity of the MLPG nodes located at the interface; therefore at the moving boundary we assume  $\hat{\mathbf{v}} = \mathbf{v}$ . The QE scheme is simple to implement, however, if the velocity of the MLPG nodes in the spatial flow domain  $\hat{\mathbf{v}}$  (which is only a function of the rate of displacement of the nodes at the moving surface), is neglected, the accuracy of the flow field results will strongly depend on this assumption. An estimation of the errors associated by assuming negligible the velocity of the nodes  $\hat{\mathbf{v}}$  in the flow domain, and the formal study about the conditions under which this assumption is valid, have not been performed in this research. However, further investigation is being carried out by the authors in which the QE approach results are being compared with results obtained by using a complete Arbitrary Lagrangian-Eulerian formulation. In the computer implementation of the ALE technique, it is necessary to formulate a procedure to update, at each time step  $n + 1$ , the position vector  $\mathbf{X}^{n+1}$  of the MLPG nodes located in the flow domain, in the vicinity of the moving surfaces, as a function of the prescribed *a priori* displacement vector  $\mathbf{u}_b$  of the nodes located at the moving boundary. Once the motion of the nodes at the moving interface is known, the rezoning of the MLPG nodes in the flow domain is determined by using an automatic nodes-displacement procedure, which is based on the solution of an elliptic (elastostatic) model. The solution of the elliptic model provides the displacement vector  $\mathbf{u}$  of the MLPG nodes located in the flow domain. As it is well known, the major drawback of the elastostatic solution is that it does not guarantee the absence of overlapping of the nodes as the motion of the surface evolves. In the elasticity approach, the spatial flow domain is assumed to be an elastic continuum. Therefore we assume that the nodes are embedded in a continuous elastostatic medium. The elastic medium analogy, which has also been implemented in the mesh based methods, considers that the elastostatic equilibrium equations together with the compressive and shear moduli of the medium, define the grid deformation. For large deformation problems using mesh based methods, the elasticity method is normally associated with some type of re-

meshing. Sophisticated elastic analogy methods have been developed in which the material properties of the elastic continuum are functions of the cell characteristics, in such a manner that the mesh material stiffness may be proportional to the cell aspect ratio, therefore the deformation of the mesh near the moving boundary may be less than the deformation of the cells away from the solid-fluid interface. The elasticity analogy models have also been implemented with nonlinear stress-strain relationships that allow to control the degree of mesh distortion [Stein, Tezduyar, and Benney (2003); Barone and Payne (2005)].

The linear elastostatic methods for the repositioning of the mesh (MLPG nodes) are based on two fundamental assumptions: (i) the geometrical linearization, in which it is assumed that the infinitesimal strain tensor  $\epsilon_{ij}(\mathbf{u})$ , is given by

$$\epsilon_{ij}(\mathbf{u}) = \frac{1}{2} \left( \frac{\partial u_i}{\partial x_j} + \frac{\partial u_j}{\partial x_i} \right), \quad (22)$$

note that nonlinear strain terms  $(\partial u_k / \partial x_i)(\partial u_k / \partial x_j)$  have been neglected in Eq. (22), and (ii) the material behaves linearly, that is the stress tensor  $\sigma_{ij}$  is given by the relationship  $\sigma_{ij} = C_{ijkl}\epsilon_{kl}$ , where the coefficients  $C_{ijkl}$  may depend on space, but they do not depend on the deformation. Both assumptions are valid for infinitesimal small deformations of the continuum. Using the MLPG approach each of the nodes located at the moving surface may have large independent displacements compared to the size of the flow domain, in which case (such as the cases shown in Sects. 7.2, 7.3 and 7.4), the continuous medium in which the MLPG nodes are embedded, may be considered as a hyperelastic material. The hyperelasticity theory takes into account constitutive laws to model materials that respond elastically up to very large strains with nonlinear kinematics and nonlinear material behaviour.

The repositioning of the nodes in the flow domain considering large displacements of the nodes at the moving interface, may be obtained by solving the hyperelasticity equations which are based on the relationship between the Green-Lagrange strain tensor  $\mathbf{E}$ , the second Piola-Kirchhoff stress tensor  $\mathbf{T}$  and the stored energy function  $W$ , i.e.

$$\mathbf{T} = \frac{\partial W}{\partial \mathbf{E}}. \quad (23)$$

The stored energy function  $W$  can be of the Mooney-Rivlin type, which is often used to model incompressible materials. The repositioning of the MLPG nodes by assuming a hyperelastic medium is a complicated task, however it is under investigation in the research group of the authors. In order to overcome the problem associated with the rezoning of the nodes we have taken into account the equations of the linear elasticity theory under the conditions of equilibrium and steady state

(the displacement of the MLPG nodes at the time step  $n + 1$  is "frozen" after the solution of the elastostatic model), and assuming that the nodes are embedded in an isotropic and homogeneous elastic medium, the equations governing the displacement  $\mathbf{u}$  of the nodes in the flow domain are written as

$$\frac{\partial \sigma_{ij}}{\partial x_i} + f_j = 0, \quad (24)$$

where  $\sigma_{ij}$  is the Cauchy stress tensor and  $f_j$  is the body force vector per unit volume. In the linear elasticity theory, the components of the stress tensor  $\sigma_{ij}$  are defined as

$$\sigma_{ij} = \lambda \operatorname{tr}(\varepsilon_{ij}(\mathbf{u})) \mathbf{I} + 2G\varepsilon_{ij}(\mathbf{u}), \quad (25)$$

where  $\operatorname{tr}()$  is the trace operator,  $\lambda$  and  $G$  are the Lamé constants, and  $\mathbf{I}$  is the identity tensor. In terms of the displacement vector  $\mathbf{u}$ , Eq. (24) is written as

$$G\nabla^2 \mathbf{u} + (G + \lambda) \operatorname{grad} \operatorname{div} \mathbf{u} + \mathbf{f} = \mathbf{0}. \quad (26)$$

We refer to Eq. (26) as the elastostatic equation. In this investigation we assume that the divergence of the displacement vector and the body force vector are negligible, hence it may be seen that the rezoning of the MLPG nodes is reduced to the solution of the Laplace equation for each component of the displacement vector. The Dirichlet boundary conditions are represented by the displacement of the MLPG nodes at the moving boundary  $\mathbf{u}_b$  and the null displacement of the MLPG nodes at the fixed boundaries. Hence the formal statement of the problem is as follows: Given  $\mathbf{u}_b$ , the prescribed displacement of the nodes located on the moving surface, find the displacement field  $\mathbf{u}$  of the nodes located on the flow domain such that

$$\nabla^2 \mathbf{u} = \mathbf{0} \quad \text{in the flow domain,} \quad (27)$$

$$\mathbf{u} = \mathbf{u}_b \quad \text{on the moving boundary and} \quad (28)$$

$$\mathbf{u} = \mathbf{0} \quad \text{on the fixed boundary.} \quad (29)$$

Eqs. (27)-(29) are, respectively, the governing equation, the moving and the fixed boundary conditions. The Laplace equation, see Eq. (27), along each direction is also solved by the MLPG method, hence the local weak formulation of Eq. (27) is represented as

$$\int_{\Omega_s} (\nabla \cdot \nabla u_i) w d\Omega = 0, \quad (30)$$

where the subindex  $i$  goes from 1 to 3. Using the divergence theorem, Eq. (30) may be written as

$$\int_{\Omega_s} \left( \frac{\partial u_i}{\partial x_1} \frac{\partial w}{\partial x_1} + \frac{\partial u_i}{\partial x_2} \frac{\partial w}{\partial x_2} + \frac{\partial u_i}{\partial x_3} \frac{\partial w}{\partial x_3} \right) d\Omega - \int_{\Gamma_s} \left( w \frac{\partial u_i}{\partial x_1} n_1 + w \frac{\partial u_i}{\partial x_2} n_2 + w \frac{\partial u_i}{\partial x_3} n_3 \right) d\Gamma = 0. \quad (31)$$

Note that an identical weight function  $w$  is used in the weak form of each of the equations (27). After the solution of the Laplace equation for each component of the displacement vector  $\mathbf{u}$ , the position of the nodes out of the moving boundaries, at the time step  $n + 1$  is calculated as

$$\mathbf{X}^{n+1} = \mathbf{u} + \mathbf{X}^n. \quad (32)$$

Once the position of the whole set of MLPG nodes in the flow domain is known at the time step  $n + 1$ , we proceed to calculate the flow field by using the iterative process described in Sect. 4.

Fig. 2 shows the flowchart of the entire process that we follow for the solution of the Navier-Stokes equations *in a fluid domain with solid-surfaces in motion*. As it has been mentioned the MLPG method has been coupled with (i) an iterative fully implicit approach, (ii) a simplified version of the ALE formulation (the QE model) for tracking the moving surface, and (iii) an elliptic elastostatic procedure for repositioning the MLPG nodes in the flow domain.

## 6 Isoparametric mapping and the MLS technique

As it has been mentioned in Sec. 2, the MLPG method is based on the local weak formulation of the governing equations. The integration of the equations is performed in a local sub-domain  $\Omega_s$  surrounding each node. Even though the computer code has been developed to obtain the numerical solution of three dimensional and non-steady fluid flow problems, in this paper we only report the solution of transient two dimensional problems with deformed geometry. The local sub-domain  $\Omega_s$  surrounding each node is a four sided deformed region defined by 9 nodes. Each of the deformed regions (defined in the Cartesian coordinate system-physical flow domain) is mapped to a standard computational region ( $-1 \leq r \leq 1$ ,  $-1 \leq s \leq 1$ ) defined in the local orthogonal curvilinear coordinate system  $(r, s)$ . In the local standard domain, the integration of the equations is carried out by a Gauss-Lobatto-Legendre quadrature rule. We have approximated all the dependent variables of the system ( $v_j$ ,  $p$ ,  $v'_j$ ,  $p'$ ,  $T$  and  $u_j$ ) by a polynomial expansion of the form

$$u^\delta(x_1, x_2) = \sum_{i=1}^{N=9} \phi^i(r, s) u^i(x_1, x_2), \quad (33)$$

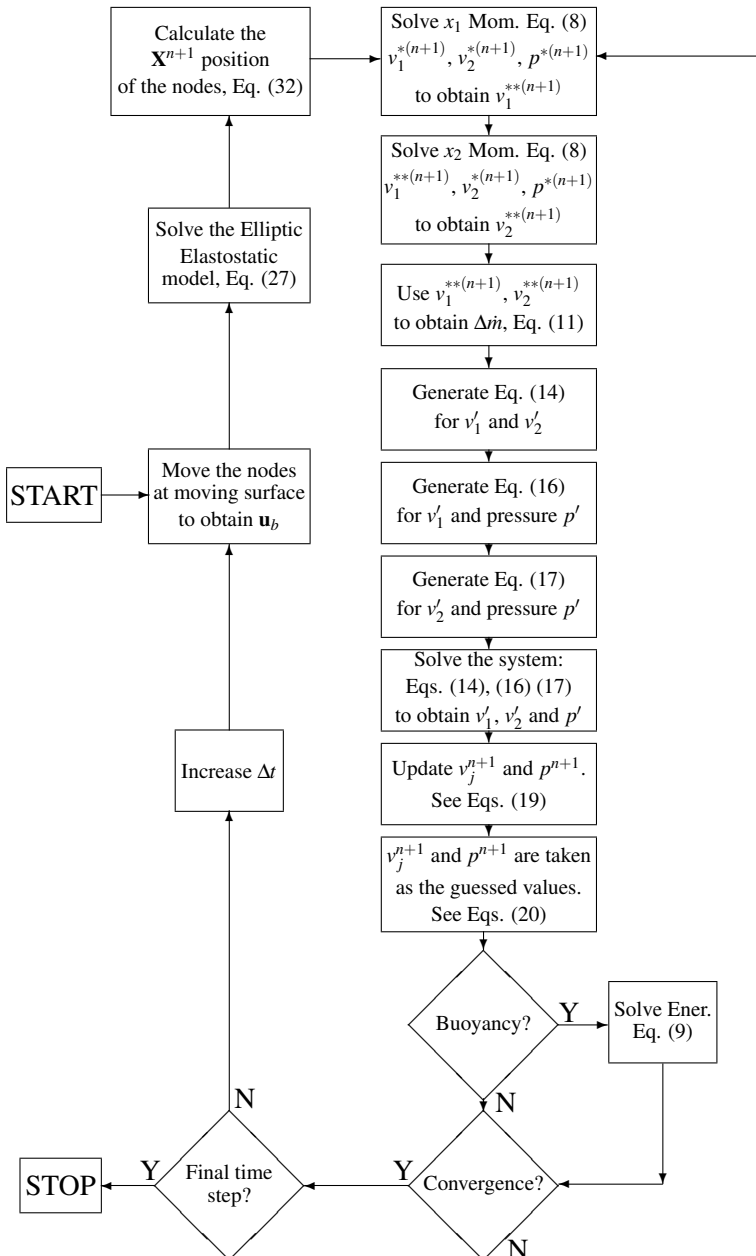


Figure 2: Flowchart: MLPG solution of the Navier-Stokes equations coupled with: (i) a fully implicit pressure correction approach, (ii) an ALE formulation, and (iii) an elliptic elastostatic model.

where  $x_1, x_2$  are the Cartesian coordinates and  $r$  and  $s$  are the local orthogonal curvilinear coordinates defined in the standard region. The summation is carried out over the local region  $\Omega_s$  defined by the number of neighbours ( $N = 9$ ) surrounding each node. The shape functions  $\phi^i(r, s)$  defined in the standard region are digitally generated by using the Moving Least Squares (MLS) numerical technique. In the MLPG method the domain surrounding each node may be of an arbitrary shape. The shape of this region is defined by the position of the nodes in the neighbourhood of each node used to discretize the domain. To integrate or differentiate the dependent variables in regions with deformed geometry we introduce a one-to-one mapping between the Cartesian coordinate system and the orthogonal curvilinear coordinate system. The mapping used is based upon the MLS shape functions  $\phi^i(r, s)$  in an iso-parametric representation. Using an iso-parametric mapping, the geometry of the local region is represented with an expansion of the same polynomial order as the dependent variables, hence the geometry of the domain surrounding each node is also represented as

$$x_i = \sum_{k=1}^N \phi^k(r, s) x_i^k, \quad (34)$$

where  $x_1^k$  and  $x_2^k$  are the Cartesian coordinates of the neighbours that constitute the local domain surrounding each node. After the MLS shape functions are digitally generated, the differential and integral operations may be carried out. The MLS approximation  $u^\delta(\mathbf{x})$  of the general function  $u(\mathbf{x})$  is written as

$$u^\delta(x_1, x_2) = \mathbf{P}^T(r, s) \cdot \mathbf{a}, \quad (35)$$

where

$$\mathbf{P}^T(r, s) = [1 \quad r \quad s] \quad (36)$$

is a monomial basis of order three and

$$\mathbf{a}(\mathbf{x}) = \begin{bmatrix} a_1 \\ a_2 \\ a_3 \end{bmatrix} \quad (37)$$

is a vector of unknown coefficients. In the MLS method the coefficients  $a_j$  are determined by minimizing a weighted discrete  $L_2$ -norm

$$J(r, s) = \sum_{i=1}^N w_i(r, s) [\mathbf{P}^T(r, s) \cdot \mathbf{a} - u_i]^2, \quad (38)$$

where  $w_i(r, s)$  is the weight function associated with the  $i$ th node in the local standard domain. By minimizing Eq. (38) we obtain the expression for the coefficients  $a_j$ ;

$$\mathbf{a} = \mathbf{M}^{-1} \mathbf{B} \mathbf{u}. \quad (39)$$

Using Eq. (39) in Eq. (35), we find the expression for the MLS shape functions

$$\phi^T(r, s) = \mathbf{P}^T(r, s) \cdot \mathbf{M}^{-1} \mathbf{B}, \quad (40)$$

the matrices  $\mathbf{M}^{-1}$  and  $\mathbf{B}$  are also defined in the standard domain  $(r, s)$ . The weight function  $w_i(r, s)$  used in Eq. (38), is obtained by the tensor product of the weight functions  $w_i$  defined along each direction of the local standard coordinate system, then

$$w_i(r, s) = w_i(r)w_i(s), \quad (41)$$

where the weight functions  $w_i(r)$  and  $w_i(s)$  are fourth order functions of compact support, which are defined as

$$w_i(r) = \begin{cases} 1 - 6q_r^2 + 8q_r^3 - 3q_r^4 & \text{for } q_r = \frac{|r-r_i|}{\rho_r} \leq 1 \\ 0 & \text{for } q_r = \frac{|r-r_i|}{\rho_r} > 1 \end{cases} \quad (42)$$

and

$$w_i(s) = \begin{cases} 1 - 6q_s^2 + 8q_s^3 - 3q_s^4 & \text{for } q_s = \frac{|s-s_i|}{\rho_s} \leq 1 \\ 0 & \text{for } q_s = \frac{|s-s_i|}{\rho_s} > 1 \end{cases}, \quad (43)$$

where  $\rho_r$  and  $\rho_s$  are length scales which are related with the size of the local standard domain, and the values  $|r - r_i|$  and  $|s - s_i|$  represent the distance between the  $i$ th node and the Gauss-Lobatto-Legendre point  $(r, s)$ , used in the numerical quadrature process. The derivative of the MLS shape functions with respect to the local coordinates  $r$  and  $s$  is written as, see Eq. (40):

$$\frac{\partial \phi^T(r, s)}{\partial z_i} = \frac{\partial}{\partial z_i} (\mathbf{P}^T \mathbf{M}^{-1} \mathbf{B}) = \left( \frac{\partial \mathbf{P}^T}{\partial z_i} \mathbf{M}^{-1} \mathbf{B} + \mathbf{P}^T \frac{\partial \mathbf{M}^{-1}}{\partial z_i} \mathbf{B} + \mathbf{P}^T \mathbf{M}^{-1} \frac{\partial \mathbf{B}}{\partial z_i} \right), \quad (44)$$

where  $z_i$  is a general variable representing  $z_1 = r$  and  $z_2 = s$ . The derivative of the matrix  $\mathbf{M}^{-1}$  can be obtained as

$$\frac{\partial \mathbf{M}^{-1}}{\partial z_i} = -\mathbf{M}^{-1} \frac{\partial \mathbf{M}}{\partial z_i} \mathbf{M}^{-1}. \quad (45)$$

The derivatives of the matrices  $\mathbf{P}^T$ ,  $\mathbf{M}$  and  $\mathbf{B}$  with respect to the local variables ( $r$  and  $s$ ) involve the derivatives of the weight function  $w_i(r, s)$ . The whole set of expressions needed to obtain: (i) the derivatives of the weight function  $w_i(r, s)$  with respect to the orthogonal curvilinear coordinates  $r$  and  $s$ , (ii) the transformation functions that convert the Cartesian coordinate system to a orthogonal curvilinear coordinate system, (iii) the transformation rules to perform the spatial derivatives in the Cartesian coordinate system of the dependent variables which are defined in the local orthogonal curvilinear coordinate system, (iv) the process to carry out the numerical quadrature of the volume and surface integrals, (v) the definition of the contravariant vectors used in the line integrals and (vi) the definition of the arc length increment also needed in the line integrals, have been previously reported by [Lin and Atluri (2001); Atluri and Shen (2002a); Atluri (2004); Avila and Atluri (2009)].

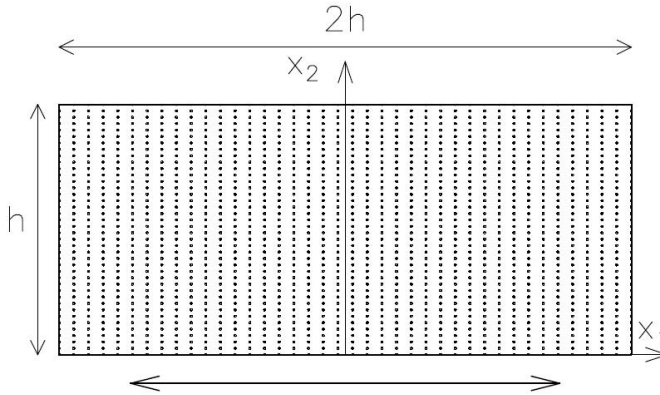


Figure 3: Non-steady flow in a periodically driven cavity flow.  $40 \times 40 = 1600$  MLPG nodes with uniform distribution. Harmonic-oscillation of the bottom lid velocity.  $St = 160$  and  $Re = 1191$ .

## 7 Results

In this section we present the numerical solutions of four cases, which have been selected mainly to show the capabilities of the MLPG methodology to solve non-steady, two-dimensional, laminar flows in fluid domains which contain solid surfaces in arbitrary prescribed spatial and temporal motions. In the first three cases the flow is confined in a rectangular cavity, whereas in the fourth case the flow is confined in a semi-cylindrical container. In the cases under study, the non-steady

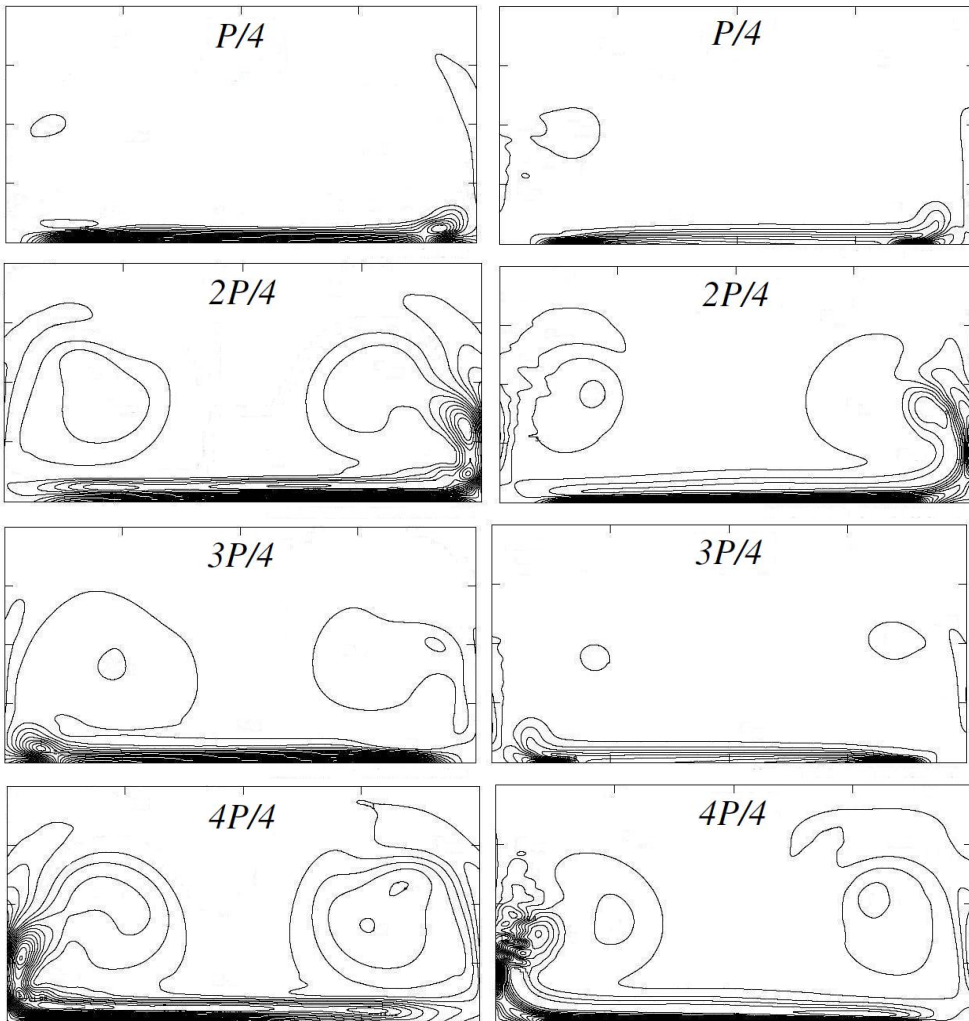


Figure 4: Non-steady flow in a periodically driven cavity flow.  $\omega_3$  vorticity fields at  $P/4$  phases of the third forcing period from rest.  $St = 160$  and  $Re = 1191$ . Left column: MLPG results ( $40 \times 40 = 1600$  MLPG nodes). Right column: SEM results.

flow field is induced by: (1) a harmonic motion of the bottom lid of the cavity, (2) a rigid flapping plate (with harmonic variation of its temperature) immersed in the fluid, (3) an undulatory elastic body immersed in the fluid, and (4) a contraction-expansion of an elastic body immersed in the fluid. The obtained results for the

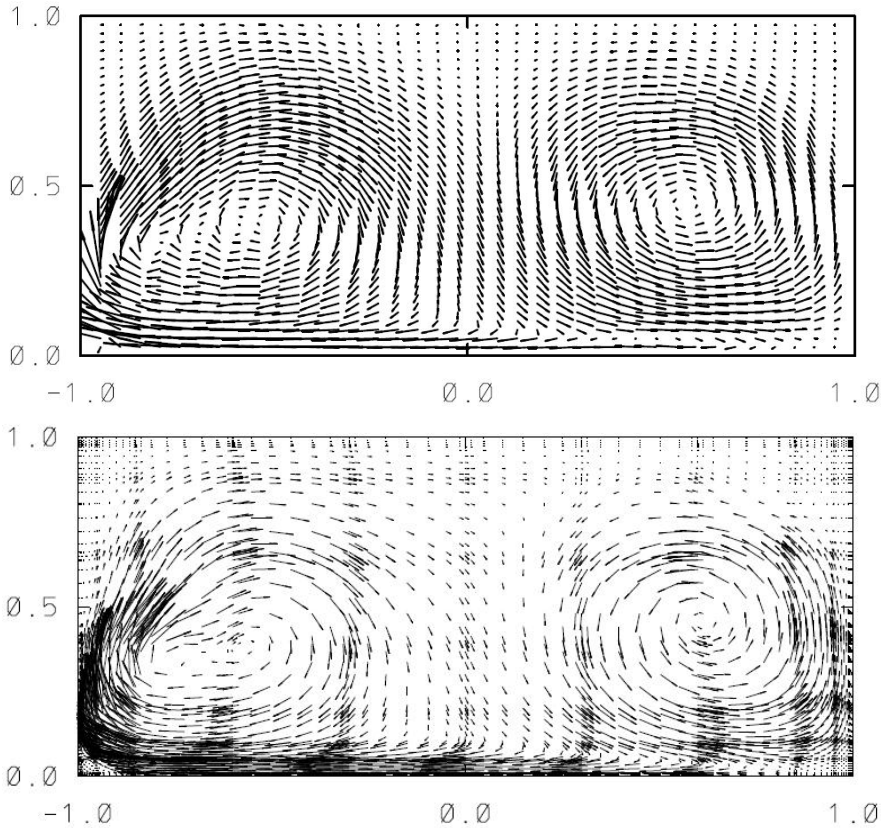


Figure 5: Non-steady flow in a periodically driven cavity flow.  $St = 160$  and  $Re = 1191$ . Velocity field at the end of the third forcing period,  $4P/4$ . Top panel: MLPG results ( $40 \times 40 = 1600$  MLPG nodes). Bottom panel: SEM results.

case with a sliding boundary (case 1) have been compared with the results provided by the mesh based spectral element method (SEM). The results of the other cases, in which rigid or elastic surfaces in arbitrary motion are present, have been qualitatively compared with observations available in the literature.

### 7.1 Non-steady flow in a periodically driven cavity flow

Two-dimensional flow calculations in a rectangular cavity whose bottom wall slides at a simple harmonic oscillation speed were carried out by [Blackburn and Lopez (2003)]. The purpose of those calculations was to generate the two dimensional, periodic in time, base flow for stability analysis and to investigate the three-dimensional

instabilities that break the space-time symmetries of the system. Fig. 3 shows the system under study. The rectangular cavity has an aspect ratio of 2 : 1 and the flow is driven by a prescribed harmonic-oscillation of the  $v_1$  velocity of the bottom lid, given by

$$v_1(x_1, 0, t) = V_{max} \sin(2\pi t/P), \quad (46)$$

where  $V_{max}$  is the amplitude of the velocity,  $t$  is the time and  $P$  is the period of the oscillation. The flow in the cavity is governed by two dimensionless parameters, since both the amplitude and frequency ( $\omega = 2\pi/P$ ) of the wall motion can be varied independently. One of these parameters is the Reynolds number which is defined as  $Re = V_{max}h/\nu$ , where  $h$  is the height of the cavity (along the  $x_2$  direction) and  $\nu$  is the kinematic viscosity of the fluid. The other controlling parameter is the Stokes number which is defined as  $St=h^2/P\nu$ . Non-slip velocity boundary conditions are imposed at the walls. The velocity is zero on the lateral and top walls. In the numerical calculations the  $x_1$  component of the velocity  $v_1$  on the oscillating bottom lid is set to [Blackburn and Lopez (2003)]:

$$v_1(x_1, 0, t) = [1 - \exp(-200(1+x_1/h)^4)][1 - \exp(-200(1-x_1/h)^4)] V_{max} \sin(2\pi t/P), \quad (47)$$

where the exponential terms lead to a smooth change of the discontinuity where the bottom lid meets the vertical stationary walls. As the  $Re$  number is increased beyond a critical value, the basic state loses its stability, and the onset of three dimensional unstable modes occurs. We have selected the value of the control parameters as  $St = 160$  and  $Re = 1191$ . These values correspond to the critical parameters leading to a three-dimensional long wavelength synchronous instability. Our numerical code solves the dimensional fluid equations; therefore in order to obtain the critical value of the control parameters, we have to propose the values of the fluid properties and the length scale of the cavity. The selected values that satisfy the critical parameters ( $St = 160$  and  $Re = 1191$ ) are the following:  $\rho = 1 \text{ kg/m}^3$ ,  $\mu = 0.0042 \text{ kg/m-s}$ ,  $P = 1.488 \text{ s}$ ,  $V_{max} = 5 \text{ m/s}$  and  $h = 1 \text{ m}$ . In the numerical solution, the time increment was fixed to  $\Delta t = 0.05 \text{ s}$ . [Vogel, Hirsra, and Lopez (2003); [Blackburn and Lopez (2003)] found that the two-dimensional time periodic basic state consists of large scale rotating flow structures that form alternately at each end of the cavity, synchronously with the stroke of the bottom lid. Instantaneous contours of the  $\omega_3$  vorticity at  $P/4$  phases of the third forcing period (from rest) of the bottom lid motion, are shown in Fig. 4. On the left column the MLPG results are shown, whereas on the right column the SEM results are presented. The SEM results were obtained by using a mesh of 108 macro elements ( $12 \times 9$ ). The

shape functions of the dependent variables in the SEM approach were generated as tensor products of a polynomial nodal expansion based on Lagrange polynomials. The order of the one-dimensional Lagrange interpolants was selected to be equal to 9. The Lagrange polynomials are associated with nodal points located at the zeros of the Gauss-Lobatto-Legendre polynomials [Karniadakis and Sherwin (1999); Rønquist (1988)]. Fig. 4 shows that at  $2P/4$  and  $4P/4$  the flow pattern exhibits two large-scale vortices which are generated by the presence of the vertical walls. It is observed that at  $P/4$  and  $3P/4$  most of the vorticity is concentrated within the Stokes layer adjacent to the oscillating wall. Note that the vorticity field and the core position of the large scale vortices (at  $2P/4$  and  $4P/4$ ) obtained by the MLPG method are in fair agreement with the results provided by the SEM. Tab. 1, shows the maximum  $\omega_3$  vorticity (clockwise rotation) at  $P/4$  phases of the third forcing period. Within each parenthesis we have written three numbers; the first two numbers correspond to the coordinates  $x_1$  and  $x_2$  of the point where the maximum  $\omega_3$  vorticity takes place. The third number represents the value of the maximum  $\omega_3$  vorticity. Tab. 2, shows the minimum  $\omega_3$  vorticity (counterclockwise rotation) at the  $P/4$  phases of the third forcing period, again; within each parenthesis we have written the coordinates of the point (where the minimum value occurs), and the value of the minimum  $\omega_3$  vorticity. Regarding the maximum vorticity and the position where it takes place, at  $2P/4$ , it is observed that both methods provide very similar results. On the other hand, note that at  $4P/4$ , the values of the minimum  $\omega_3$  vorticity and the position where it occurs, obtained by both methods, are in fair agreement.

Table 1: Maximum  $\omega_3$  vorticity [ $s^{-1}$ ] (clockwise), and position where it occurs, at  $P/4$  phases of the third forcing period, see Fig. 4. ( $x_1, x_2, \omega_{3max}$ ).

	$P/4$	$2P/4$	$3P/4$	$4P/4$
MLPG	(-0.58,0.01,109.4)	(0.89,0.3,21.2)	(-0.84,0.01,33.6)	(-0.74,0.01,34.5)
SEM	(-0.67,0.01,321.8)	(0.8,0.38,24.1)	(-0.77,0.01,156.0)	(-0.58,0.01,116.3)

Table 2: Minimum  $\omega_3$  vorticity [ $s^{-1}$ ] (counterclockwise), and position where it occurs, at  $P/4$  phases of the third forcing period, see Fig. 4. ( $x_1, x_2, \omega_{3min}$ ).

	$P/4$	$2P/4$	$3P/4$	$4P/4$
MLPG	(0.84,0.01,-32.5)	(0.64,0.01,-47.1)	(0.58,0.01,-109.1)	(-0.89,0.28,-23.8)
SEM	(0.77,0.01,-154.3)	(0.6,0.01,-138.1)	(0.67,0.01,-319.3)	(-0.8,0.36,-25.5)

The velocity field at the end of the third forcing period,  $4P/4$ , is shown in Fig. 5.

It may be seen that the MLPG method is capable of properly calculating the core location of the two large-scale rotating flow structures. Tab. 3 shows the maximum and minimum value of the horizontal  $v_1$  and vertical  $v_2$  velocities, at the end of the forcing period, see Fig. 5. It may be observed that the values obtained by the two methods are of the same order of magnitude. Tab. 4 shows the coordinates  $(x_1, x_2)$  of the point where the maximum value of the velocities,  $v_1$  and  $v_2$ , take place. Regarding the maximum  $v_2$  velocity and the location where it takes place, note that the results obtained by both methods are in fair agreement. We may conclude that the MLPG method is a reliable numerical algorithm that is capable of solving non-steady, two-dimensional, laminar flows driven by an oscillatory motion of the bottom lid of a rectangular cavity.

Table 3: Maximum and minimum value of the velocities [m/s] at the end,  $4P/4$ , of the third forcing period, see Fig. 5 .

	$v_{1max}$	$v_{1min}$	$v_{2max}$	$v_{2min}$
MLPG	0.88	-1.85	2.04	-0.63
SEM	1.04	-1.71	1.84	-0.54

Table 4: Maximum value of the  $v_1$  and  $v_2$  velocities [m/s] and position where they take place, at the end,  $4P/4$ , of the third forcing period, see Fig. 5.  $(x_1, x_2, v_{imax})$

	$v_{1max}$	$v_{2max}$
MLPG	(0.53, 0.12, 0.88)	(-0.94, 0.25, 2.04)
SEM	(-0.83, 0.44, 1.04)	(-0.93, 0.3, 1.84)

## 7.2 Non-steady flow surrounding a rigid flapping plate with time-periodic temperature

The unsteady fluid motion induced by a flapping wing either rigid or flexible, has been the subject of numerous investigations. In the aircraft industry, aeronautical engineers have observed that a rigid flapping airfoil can generate "dynamic stall". This term has been used to describe the fluid dynamics phenomenon that is capable of generating delay of stall on wings and airfoils that are rapidly pitched beyond the static stall angle [Carr and Chandrasekhara (1996)]. In nature, it has been observed by biofluid-dynamicists that the non-steady flow induced by continuously flapping flexible wings, possess the optimal aerodynamic features for the efficient unsteady flight of small birds and insects [Ho, Nassef, Pornsinsirak, and Tai (2003)]. In

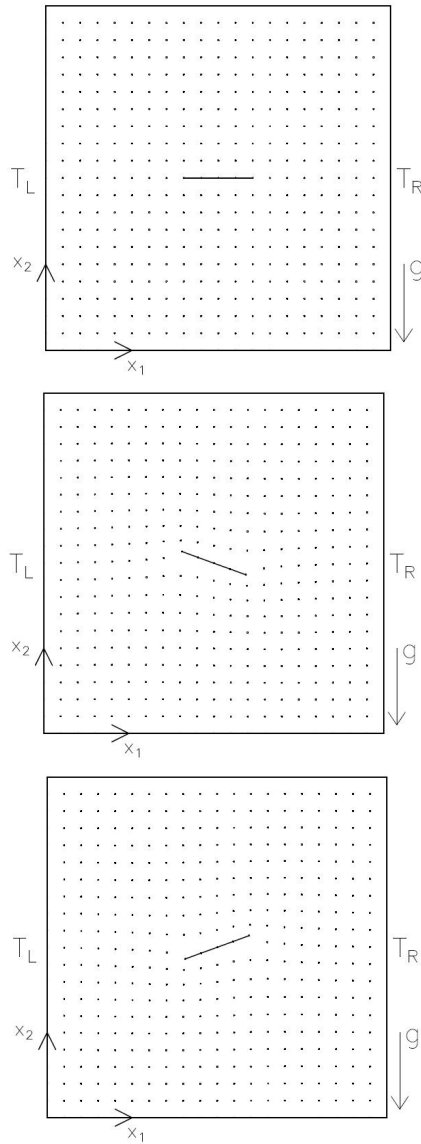


Figure 6: Non-steady flow surrounding a flapping plate with time-periodic temperature variation. 21x21 MLPG nodes. Harmonic-oscillation of the plate with angular position:  $\theta = A \cos(2\pi t/P + \pi/2)$ . Top panel:  $\theta = 0^\circ$ . Central panel:  $\theta = -20^\circ$ . Bottom panel:  $\theta = 20^\circ$ .

the development of micro air vehicles (MAV), the design criteria normally take

into account the flow parameters, that govern the flight of small birds, such as wing motion, unsteady flow and low Reynolds number regime [Shyy, Berg, and Ljungqvist (1999)]. The modeling and solution of the unsteady flight of natural flyers is a very complicated task and presents several unsurmountable problems, however Ellington (1984) has mentioned that the mean wing thickness of the insects is typically about 0.057% of the wing length, therefore it is reasonable to assume, as a first approximation to most insect wings, a rigid wing of negligible thickness and flexibility.

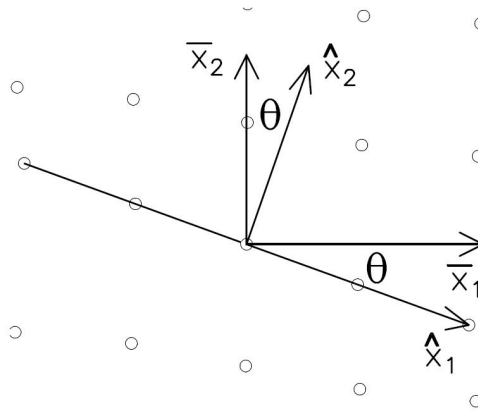


Figure 7: Non-steady flow surrounding a flapping plate with time-periodic temperature variation. Definition of the local coordinate systems. A fixed reference frame  $(\bar{x}_1, \bar{x}_2)$  and a rotating reference frame  $(\hat{x}_1, \hat{x}_2)$ . Harmonic-oscillation of the plate with angular position:  $\theta = A \cos(2\pi t/P + \pi/2)$ . MLPG nodes surrounding the rigid plate are also shown.

In this section we use the approximation proposed by Ellington (1984) (a plate of negligible thickness and flexibility) to calculate, by using the MLPG method, the velocity, vorticity and temperature fields, of the flow surrounding a rigid flapping plate immersed in a quiescent fluid. The fluid is confined in a square enclosure and the flow is driven by both; (i) the non-steady normal and shear forces generated by the motion of the plate (whose length is  $l_{plate}$ ), and (ii) the non-steady buoyancy force generated by the time-periodic temperature variation of the plate. The system under study is depicted in Fig. 6. The left and right vertical sidewalls are kept at constant temperature  $T_L$  and  $T_R$  respectively (in this investigation we have assumed  $T_L = T_R$ ), while the top and bottom horizontal walls are thermally insulated. Non-slip velocity boundary conditions have been assumed on all the walls of the

enclosure and on the plate, therefore the fluid in contact with the plate acquires the instantaneous local velocity of the rigid body. The angular position  $\theta$  of the plate is given by the following cosinoidal function of time

$$\theta = A \cos(2\pi t/P + \pi/2), \quad (48)$$

where  $A$  is the amplitude of the motion ( $A = 20^\circ$ ), see Fig. 6,  $t$  is the time and  $P$  is the period. The temperature of the plate is given by the following function of time

$$T_{plate} = \bar{T} + T_{max} \cos(2\pi t/P_T), \quad (49)$$

where  $\bar{T}$  is the mean temperature,  $T_{max}$  is the amplitude and  $P_T$  is the thermal period. The governing parameters of the system are the flapping Strouhal number ( $Str = \omega l_{plate}^2/\nu = 0.1$ ), where  $\omega = 2\pi/P$  is the frequency of the plate, and the Rayleigh number ( $Ra = \beta g \Delta T L^3/\nu \alpha = 392.4$ ), where  $L$  is the side length of the container and  $\Delta T = 2T_{max}$ . In order to satisfy the governing parameters ( $Str = 0.1$  and  $Ra = 392.4$ ) we have selected the following fluid properties, thermal conditions and geometrical parameters:  $\rho = 1 \text{ kg/m}^3$ ,  $\mu = 1 \text{ kg/m-s}$ ,  $\alpha = 1 \text{ m}^2/\text{s}$ ,  $\beta = 1 \text{ K}^{-1}$ ,  $g = 9.81 \text{ m/s}^2$ ,  $L = 1 \text{ m}$ ,  $l_{plate} = 0.2 \text{ m}$ ,  $T_L = T_R = 5^\circ\text{C}$ ,  $A = 20^\circ$ ,  $P = 10 \text{ s}$ ,  $\bar{T} = 20^\circ\text{C}$ ,  $T_{max} = 20^\circ\text{C}$ , and  $P_T = 1 \text{ s}$ . In the numerical simulation the time increment was fixed to  $\Delta t = 0.1 \text{ s}$ . To generate the motion of the nodes located at the plate and to obtain the boundary conditions for the solution of both; the fluid equations and the elliptic elastostatic model, we define a local fixed reference frame  $(\bar{x}_1, \bar{x}_2)$  whose origin is located at the center of the plate, see Fig. 7. Additionally we define another local reference frame  $(\hat{x}_1, \hat{x}_2)$  that rotates with the plate and whose origin is also located at the center of the plate, see Fig. 7. Based on these two reference frames the position vector of each node on the plate at the time step  $n+1$  is given by

$$\hat{\mathbf{x}}^{n+1} = \mathbf{A}^{n+1} \bar{\mathbf{x}}, \quad (50)$$

where  $\mathbf{A}^{n+1}$  is the transformation matrix between the two local reference systems, which is defined as

$$\mathbf{A}^{n+1} = \begin{bmatrix} \cos \theta^{n+1} & \cos(\theta^{n+1} + \pi/2) & 0 \\ \cos(\pi/2 - \theta^{n+1}) & \cos \theta^{n+1} & 0 \\ 0 & 0 & 1 \end{bmatrix}. \quad (51)$$

Note that the vector  $\bar{\mathbf{x}}$  in Eq. (50) is defined in the fixed local coordinate system, therefore it is independent on time and it is the reference position vector of the nodes on the plate at  $t = 0$ , or at angular position  $\theta = 0^\circ$ , see Fig. 6.

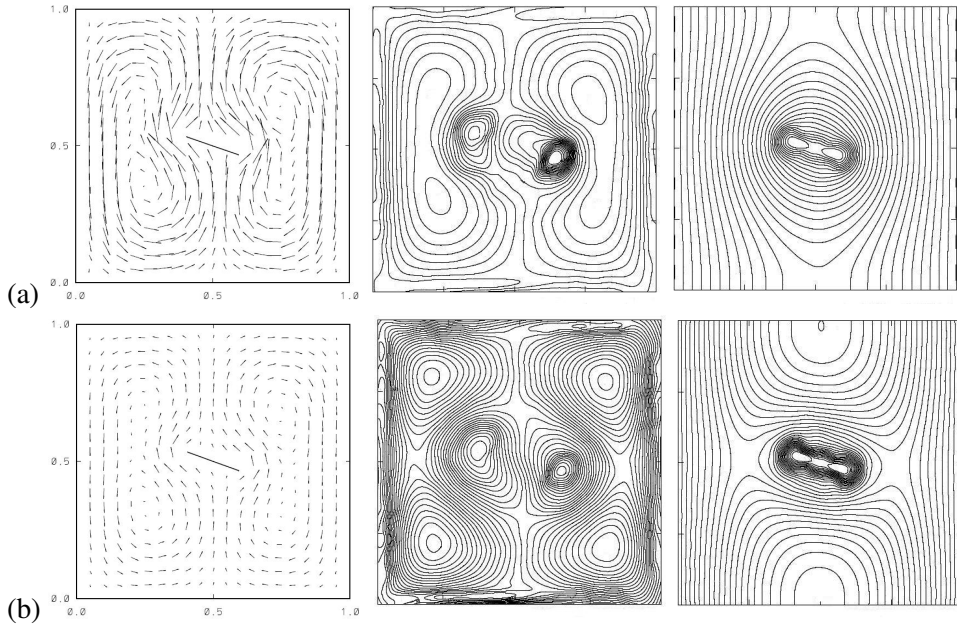


Figure 8: (a) and (b). For caption see next page.

The position of the nodes at the time step  $n + 1$  in the global Cartesian coordinate system  $(x_1, x_2)$  (whose origin is located at the bottom left of the cavity, see Fig. 6), is calculated as

$$\mathbf{x}^{n+1} = \mathbf{x}_c + \hat{\mathbf{x}}^{n+1}, \quad (52)$$

where  $\mathbf{x}_c$  is the position vector of the center of the plate (origin of the two local coordinate systems). The displacement vector at the time step  $n + 1$  of the nodes located at the plate is calculated as

$$\mathbf{u}^{n+1} = \mathbf{x}^{n+1} - \mathbf{x}^n, \quad (53)$$

where  $\mathbf{x}^n$  is the position vector of the nodes at the time step  $n$ . The displacement vector  $\mathbf{u}^{n+1}$  in Eq. (53) is taken as the boundary condition for the elliptic elastostatic model whose solution provides the displacement of the nodes located in the flow domain. The tangential velocity of the nodes located at the plate is given as  $V_T = \dot{\theta}|\mathbf{r}|$ , where the angular velocity of the plate  $\dot{\theta}$  is obtained as

$$\dot{\theta} = -\omega A \sin(\omega t + \pi/2), \quad (54)$$

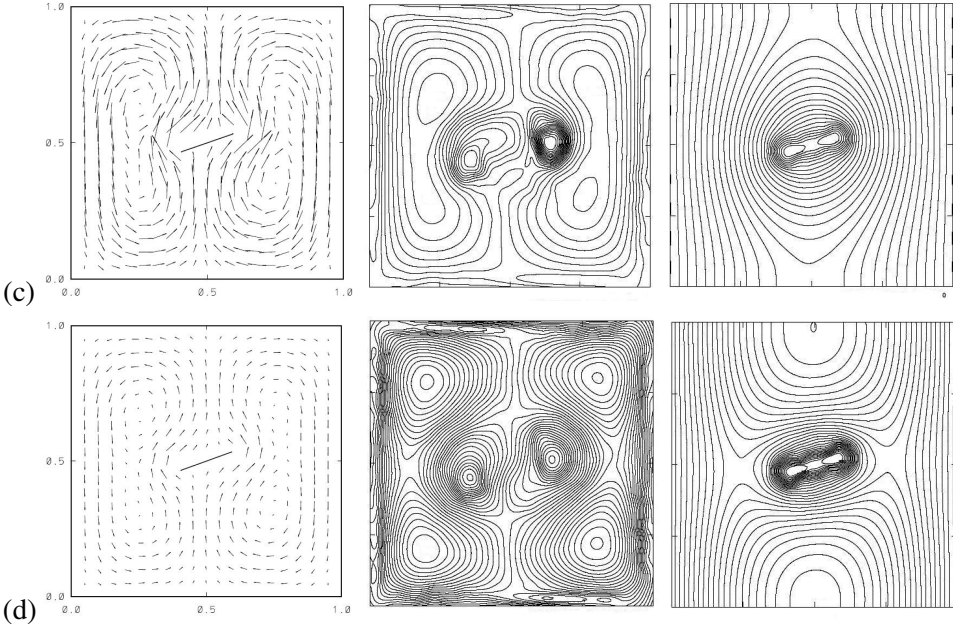


Figure 8: (c) and (d). Non-steady flow surrounding a rigid flapping plate with time-periodic temperature variation. Left column: velocity field. Central column: vorticity field. Right column: temperature field. (a)  $t = 2\text{s}$ ,  $\theta = -19.02^\circ$ ,  $T_{plate} = 40^\circ\text{C}$ ; (b)  $t = 2.3\text{s}$ ,  $\theta = -19.8^\circ$ ,  $T_{plate} = 13.8^\circ\text{C}$ ; (c)  $t = 7\text{s}$ ,  $\theta = 19.02^\circ$ ,  $T_{plate} = 40^\circ\text{C}$  and (d)  $t = 7.3\text{s}$ ,  $\theta = 19.8^\circ$ ,  $T_{plate} = 13.8^\circ\text{C}$ .

and  $|\mathbf{r}|$  is the magnitude of the position vector of the nodes in the local rotating frame of reference. Note that the tangential velocity  $V_T$  in the local rotating coordinate system is directed along the  $\hat{x}_2$  direction (normal to the plate). The velocity of the nodes located on the plate in the global Cartesian coordinate system is obtained by applying a backward transformation of the form

$$\mathbf{v} = \mathbf{A}^T \hat{\mathbf{v}}, \quad (55)$$

where the vector  $\hat{\mathbf{v}}$  has the components  $[0, V_T]$  and  $\mathbf{A}^T$  is the transpose of the transformation matrix. The velocity vector in Eq. (55), is taken as the boundary condition on the plate for the solution of the fluid equations. Fig. 8 shows the velocity, vorticity and temperature fields of the induced flow surrounding a rigid flapping plate. Note that as the temperature of the plate is increased Fig. 8 (a), the driven buoyancy force is enhanced and it leads to an increase of the fluid velocity. In the central panel of Fig. 8 (a), it is observed that two large well defined vortices

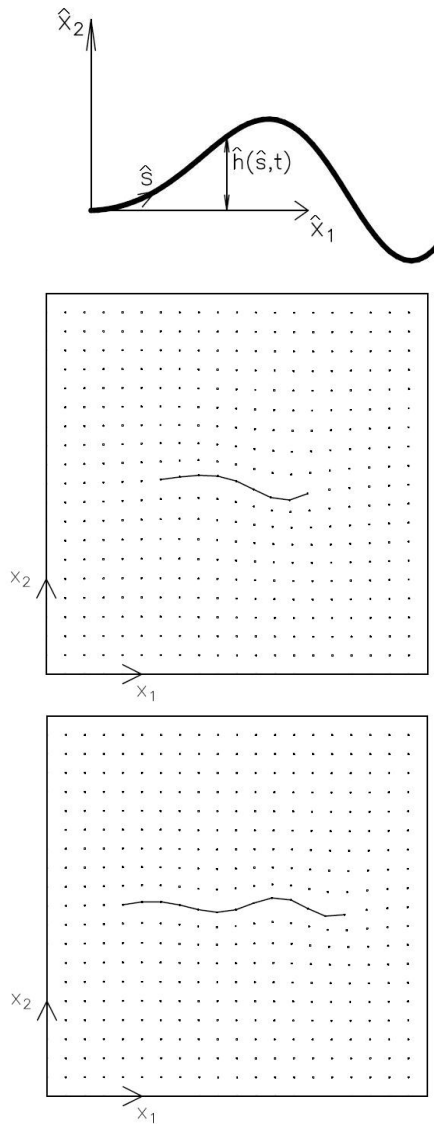


Figure 9: Non-steady flow induced by an undulating body. 21x21 MLPG nodes. Top panel: Transversal oscillation of the midline of the body (bold line) in the form of a wave traveling backwards along the body. Central panel: wave number  $k/2\pi = 1$  and amplitude at the tail  $\hat{h}_1 = 0.05$  m. Bottom panel wave number  $k/2\pi = 2$  and amplitude at the tail  $\hat{h}_1 = 0.03$  m.

are generated, the large flow structures are delimited by the walls of the enclosure. Additionally, it is seen that two small vortices appear surrounding the edges of the plate. The vorticity in Fig. 8 (a) is in the range  $-9.2\text{s}^{-1} \leq \omega_3 \leq 9.3\text{s}^{-1}$ . In the right panel of Fig. 8 (a), it is observed that due to the convective velocity, the isotherms are deformed particularly in the region occupied by the plate. It is also observed that the MLPG method successfully satisfies the Neumann boundary condition on the insulated top and bottom walls. Fig. 8 (b) shows that as the temperature of the plate is diminished, the velocity of the fluid decreases and the vorticity field is characterized by the presence of six weak vortices ( $-0.45\text{s}^{-1} \leq \omega_3 \leq 0.44\text{s}^{-1}$ ). In Fig. 8 (b) right panel, it may be seen that the temperature field resembles a pure conductive regime (see the flat distribution of the isotherms) that is only disturbed by the flow induced by the motion of the plate. Again it is observed that the MLPG method satisfies the Neumann boundary condition at the top and bottom walls. Figs. 8 (c) and (d), show the same profiles as Figs. 8 (a) and (b) respectively, but a half-period evolution in time later. Note that as the plate moves from  $\theta = -19.02^\circ$  and  $\theta = -19.8^\circ$  to  $\theta = 19.02^\circ$  and  $\theta = 19.8^\circ$  respectively, similar flow patterns are generated, however the position of the vortices and the distribution of the isotherms is modified by the motion of the plate. It is intuitive to believe that oscillating a plate immersed in a quiescent fluid will increase the heat transfer rate from its surface. It has been reported that the heat transfer from the surface of an oscillating cylinder immersed in a tank of water is increased up to 400 percent compared to that of pure free convection (static cylinder) [Martinelli and Boelter (1938)]. Further investigation will be carried out by the authors in order to evaluate the instantaneous average Nusselt number on the plate, as a function of the amplitude and frequency of the oscillating rigid body. In the light of the previous results, the authors may infer that the MLPG method is also a reliable approach that can be used to calculate the flow and heat transfer rate induced by a flapping plate located in a quiescent fluid.

### 7.3 Non-steady flow induced by an undulating body

The hydromechanics of aquatic animal propulsion is a subject that has been deeply studied by biofluid-dynamicists researches and by hydrodynamics engineers. During millions of years of animal evolution, natural swimmers have inevitably developed refined means of generating fast movement at low energy cost. Practically all of the aquatic animals that possess an efficient mobility propel themselves by undulatory motions [Lighthill (1960); Lighthill (1969); Lighthill (1970)]. In the undulatory mode of propulsion, the animals (who have the whole body flexible) when swimming, pass down their body, from head to tail, transverse waves with amplitude increasing towards the rear. In the literature, analyses of the pure undu-

latory mode of propulsion (described as "anguilliform"), in which the whole body participates, have been carried out by using Lighthill's "elongated-body" theory [Lighthill (1970)]. Based on this theory, which is valid for moderate amplitude of undulation, and for relatively elongated animals, the propulsive effectiveness of waves of lateral displacement, propagated at a given speed along the body, can be estimated. Of primary importance in the study of undulatory swimming, is the evaluation of the drag and thrust forces exerted by the fluid on the animal. Following Lighthill's "elongated-body" theory we assume, in the cases analyzed in this section, that the lateral movements of the fish midline are small compared with its length. We present the velocity and vorticity fields created by two modes of undulatory motion. In the first mode we assume that the fish (represented as an undulating filament) requires the development of a complete wave along its body for swimming (fish and eels swimming mode), whereas in the second mode we assume that the animal (represented again as an undulating filament) requires the development of two complete waves along its body for swimming (snakes mode of swimming).

The system under study is depicted in Fig. 9. We assume that the midline of the undulating body is making a transversal oscillation in the form of a wave traveling backwards along the body, i.e. along the  $\hat{x}_1$  direction of a local coordinate system whose origin is located at the front of the body, see Fig. 9 (top panel). The amplitude of the wave increases with the distance from the front of the body. The standard analyses of fish swimming take into account analytical approximations for the displacement (along the  $\hat{x}_2$  direction) of the midline  $\hat{h}(\hat{s}, t)$  of the body, where  $\hat{s}$  is the distance measured along the midline from the nose of the fish, and  $t$  is the time. We have used the following analytical expression for  $\hat{h}(\hat{s}, t)$  which gives an approximate fit to many undulating fish [Pedley and Hill (1999)]:

$$\hat{h} = \hat{h}_1 \mathbf{R} \left\{ \left[ A \exp \left( \frac{\hat{\alpha}(\hat{s}-l)}{l} \right) - iB \left( \frac{\hat{s}}{l} \right)^{\hat{\beta}} \right] \exp \left( \frac{ik(\hat{s}-Vt)}{l} \right) \right\}, \quad (56)$$

where the symbol  $\mathbf{R}\{\dots\}$  means the real part of the complex quantity in the curly brackets, i.e.

$$\hat{h} = \hat{h}_1 \left[ A \exp \left( \frac{\hat{\alpha}(\hat{s}-l)}{l} \right) \cdot \cos \left( \frac{k(\hat{s}-Vt)}{l} \right) + B \left( \frac{\hat{s}}{l} \right)^{\hat{\beta}} \cdot \sin \left( \frac{k(\hat{s}-Vt)}{l} \right) \right], \quad (57)$$

$l$  is the total length of the body,  $k/2\pi$  represents the number of complete waves in one body length,  $V$  is the speed of the wave traveling along the fish, which is defined as  $V = 2\pi l/(kP) = \omega l/k$ ,  $P$  and  $\omega$  are the period and frequency of the tail beat of the fish respectively,  $\hat{\alpha}$ ,  $\hat{\beta}$  are measures of the rate at which the wave amplitude increases toward the tail,  $A$  and  $B$  are real constants chosen so that  $A^2 + B^2 = 1$ ,  $i$  is

$\sqrt{-1}$  and  $\hat{h}_1$  is the amplitude at the tail ( $\hat{s} = l$ ). We have used the following values:  $\hat{\alpha} = 0$ ,  $\hat{\beta} = 1$ ,  $A/B = 5/12$ . In the first case presented in this section, we use a wave number  $k/2\pi$  equal to 1, which is a typical value for fish swimming, while in the second case we use a wave number  $k/2\pi$  equal to 2, which is a characteristic value for eel swimming [Graham, Lowell, Rubinoff, and Mota (1987)], see central and bottom panels of Fig. 9. In both cases, the speed of the wave along the body has been selected as  $V = 0.03$  m/s, the amplitude at the tail for the first case is  $\hat{h}_1 = 0.05$  m, whereas for the second case is  $\hat{h}_1 = 0.03$  m. The body is immersed in a quiescent fluid confined in a square cavity whose side length  $L$  is equal to 1 m. The fluid has the following properties:  $\rho = 1$  kg/m<sup>3</sup> and  $\mu = 1$  kg/m-s. The time increment in the solution of the fluid equations was fixed to  $\Delta t = 0.5$  s. The length of the undulating body for the first case is  $l = 0.4$  m, whereas for the second case is  $l = 0.6$  m. In order to specify the boundary conditions on the undulating body to solve the elliptic elastostatic model and the fluid equations, we need to evaluate the displacement vector  $\mathbf{u}$  and the velocity vector  $\mathbf{v}$  at the time step  $n + 1$  of the MLPG nodes located on the fish. The displacement vector  $\mathbf{u}$  is obtained as follows. First, the local coordinates  $(\hat{x}_1, \hat{x}_2)$  of each node are evaluated, note that  $\hat{x}_2 = \hat{h}(\hat{s}, t)$ , however, to calculate  $\hat{x}_1$  we need to calculate the  $\hat{x}_1$  increments of the nodes located on the midline  $\hat{s}$  by the relation

$$d\hat{x}_1 = (d\hat{s}^2 - d\hat{h}^2)^{1/2}. \quad (58)$$

Once the local coordinates  $(\hat{x}_1, \hat{x}_2)$  are known, the position vector  $\mathbf{x}$  and displacement vector  $\mathbf{u}$  of the nodes located on the fish at the time step  $n + 1$ , but referred to the global Cartesian coordinate system (whose origin is located at the left bottom of the cavity, see Fig. 9), are evaluated by Eqs. (52) and (53), however this time the vector  $\mathbf{x}_c$ , is the position vector of the origin of the local coordinate system  $(\hat{x}_1, \hat{x}_2)$ . The displacement vector  $\mathbf{u}$  represents the boundary conditions for the solution of the elliptic elastostatic model.

The velocity vector of the nodes on the fish has been obtained by taking the derivative of Eq. (57) with respect the time, we obtain the velocity along the  $x_2$  direction of each node located on the midline  $\hat{s}$  as

$$v_2 = \frac{d\hat{h}}{dt} = \hat{h}_1 \left[ A \exp\left(\frac{\hat{\alpha}(\hat{s}-l)}{l}\right) \frac{kV}{l} \sin\left(\frac{k(\hat{s}-Vt)}{l}\right) - B\left(\frac{\hat{s}}{l}\right)^{\hat{\beta}} \frac{kV}{l} \cos\left(\frac{k(\hat{s}-Vt)}{l}\right) \right]. \quad (59)$$

The velocity along the  $x_1$  axis of the nodes located on the midline  $\hat{s}$  is determined numerically by using the expression

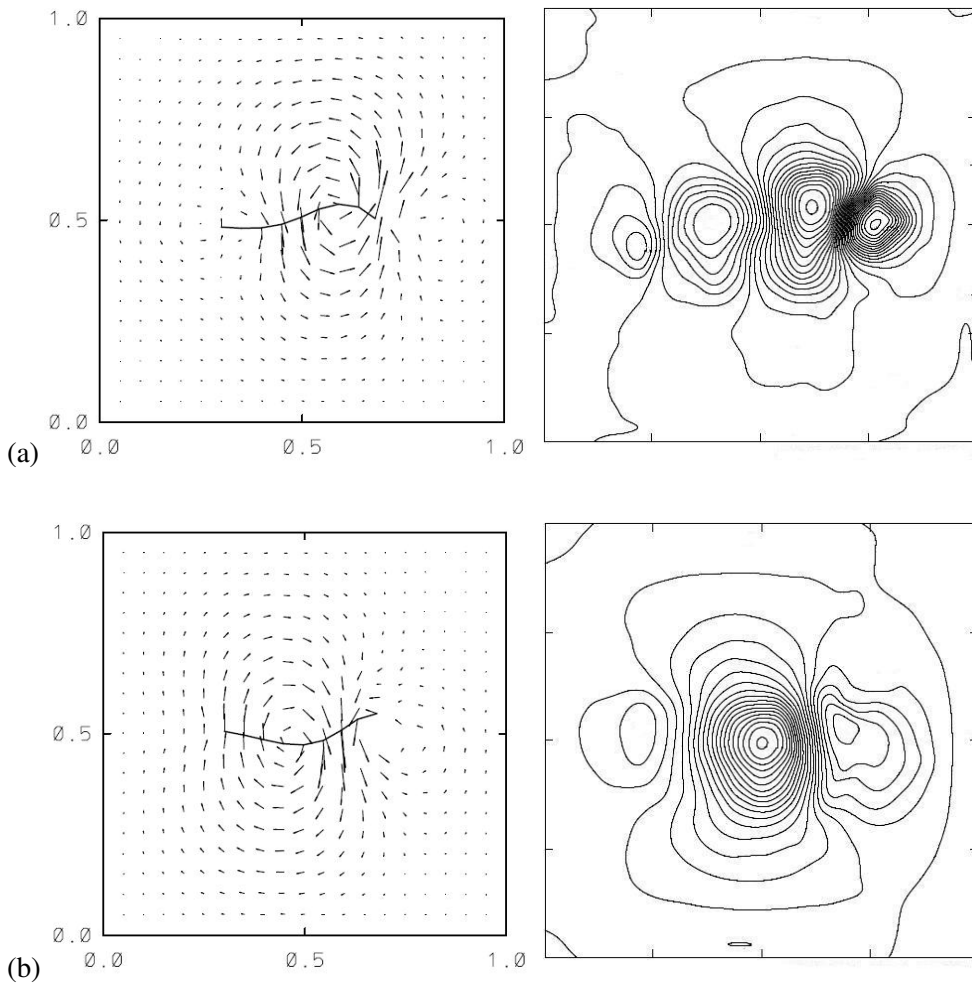


Figure 10: (a) and (b). For caption see next page.

$$v_1 = \frac{d\hat{x}_1}{dt} \approx \frac{\hat{x}_1^{n+1} - \hat{x}_1^n}{\Delta t}, \quad (60)$$

where  $\hat{x}_1^{n+1}$  and  $\hat{x}_1^n$  are the positions (in the local coordinate system) of the nodes at the current and previous time respectively.

Fig. 10 shows for the first case (wave number  $k/2\pi=1$ ) the velocity and vorticity fields at  $P/4$  phases of the tail beat period. The period  $P$  and the frequency  $\omega$  of

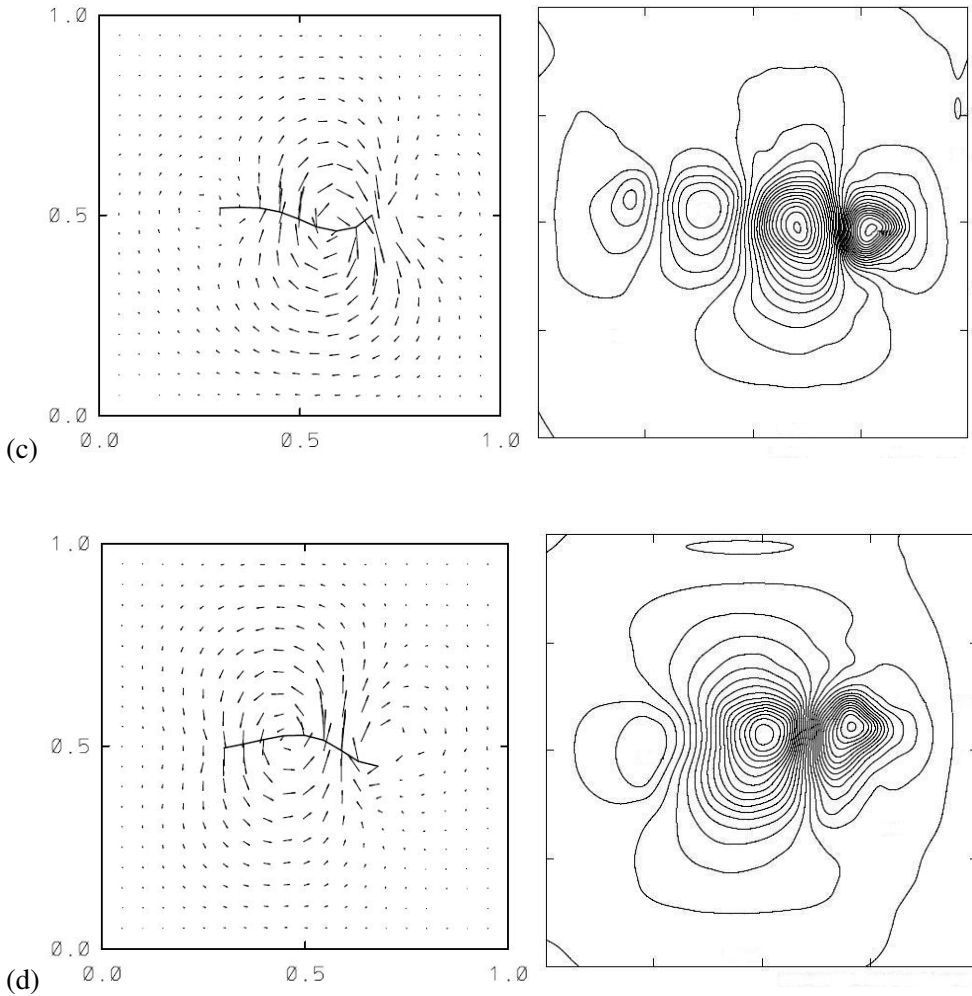


Figure 10: (c) and (d). Non-steady flow induced by an undulating body with wave number  $k/2\pi = 1$ . Velocity and vorticity fields at  $P/4$  phases of the tail beat.  $V = 0.03$  m/s, period and frequency of the tail beat,  $P = 13$  s and  $\omega = 0.48$  s<sup>-1</sup> respectively. Left column: velocity field. Right column: vorticity field. (a)  $P/4$ , (b)  $2P/4$ , (c)  $3P/4$ , (d)  $4P/4$ .

the tail beat are  $P = 13$  s and  $\omega = 0.48$  s<sup>-1</sup> respectively. It is observed that at  $P/4$ , the nose of the body (located at the left end of the filament) has a small upward velocity, while the tail has an upward motion with high velocity. It may be seen

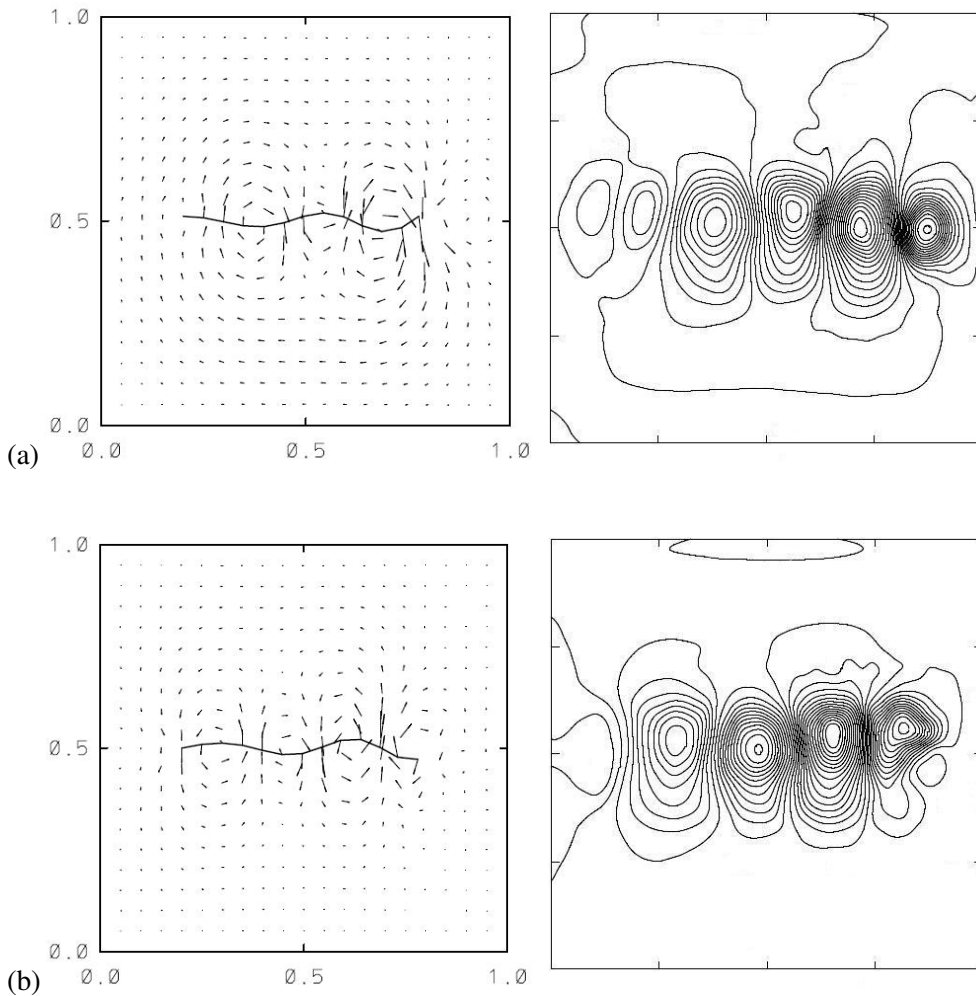


Figure 11: (a) and (b). For caption see next page.

that from the second node, from the nose, the velocity is downward, and its value first increases and then decreases close to the last section of the body. As a result of the body motion, we obtain a large counter-clockwise flow structure in the central region of the body. It is also observed that due to the small velocity of the head section, a small counter-clockwise vortex appears. The core of the small counter-clockwise vortex is located slightly in front and above the midline of the fish. In the rear region, due to the high vertical velocity of the tail, a clockwise vortex is induced. The core of this vortex is located behind and below the midline of the fish.

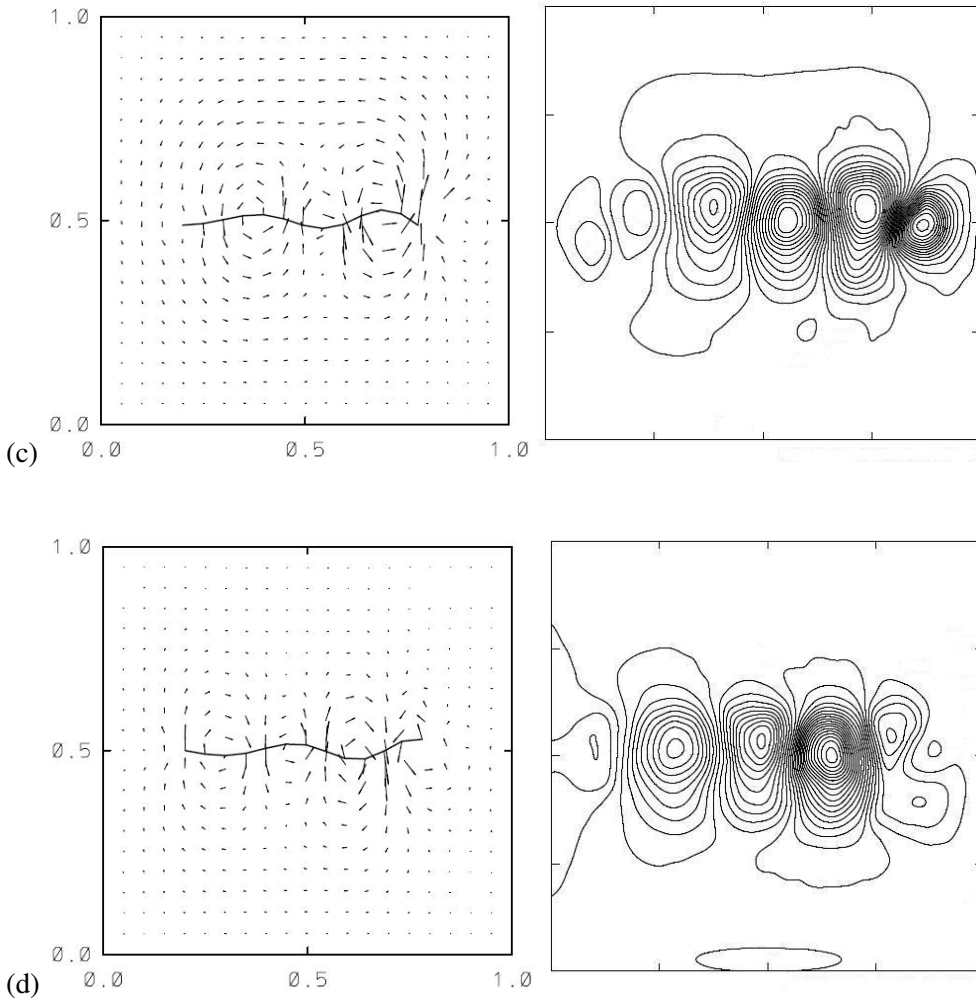


Figure 11: (c) and (d). Non-steady flow induced by an undulating body with wave number  $k/2\pi = 2$ . Velocity and vorticity fields at  $P/4$  phases of the tail beat.  $V = 0.03$  m/s, period and frequency of the tail beat,  $P = 10$  s and  $\omega = 0.62$  s<sup>-1</sup> respectively. Left column: velocity field. Right column: vorticity field. (a)  $P/4$ , (b)  $2P/4$ , (c)  $3P/4$ , (d)  $4P/4$ .

At  $P/4$  the clockwise vortex at the tail (at  $x_1 = 0.74$  m and  $x_2 = 0.51$  m), induces a vorticity  $\omega_3 = 0.27$  s<sup>-1</sup>, whereas the counter-clockwise vortex on the central part of the body region (at  $x_1 = 0.59$  m,  $x_1 = 0.5$  m), induces a vorticity  $\omega_3 = -0.28$  s<sup>-1</sup>. In

the vorticity fields shown on the right column of Fig. 10, it may be seen that at  $P/4$ , four vortices are generated, the larger structure is placed in the central part, whereas the smaller vortex is located at the tail. It is observed that due to the presence of the walls the vorticity is damped and no vortex shedding behind the body is observed. At  $2P/4$ , it is observed that the head of the body has higher upward velocity than the tail. It is seen that the upward velocity at the head monotonically decreases along the body, and at the central portion it becomes downward. The motion of the fish induces a large clockwise flow structure in the front and central part. But due to the motion at the tail a small counter-clockwise vortex is also generated. The core of this vortex is located below the middle line. It is seen that the vorticity field shows a large vortex in the central part and two small vortices at the front and at the tail. At  $2P/4$ , the clockwise vortex in the central region of the body ( $x_1 = 0.49$  m,  $x_2 = 0.5$  m), induces a vorticity  $\omega_3 = 0.24 \text{ s}^{-1}$ , whereas the counter-clockwise vortex at the tail ( $x_1 = 0.68$  m,  $x_2 = 0.44$  m), induces a vorticity  $\omega_3 = -0.2 \text{ s}^{-1}$ . Notice that the vortex at the tail is weaker than the vortex at the central part. At  $3P/4$ , it is observed that not only the nodes on the body have the negative of the vertical velocity of the nodes on the midline at  $P/4$ , but also the shape of the body has been modified, therefore we observe that the flow pattern is the inverse of the flow pattern found at  $P/4$ . It is observed that the core of the small vortex at the nose appears slightly below the midline, and the core of the vortex at the tail now appears above the midline. The vorticity values and the place where they occur are very similar to those found at  $P/4$ . At  $4P/4$ , it is once again observed that not only the nodes on the body have the negative of the vertical velocity of the nodes on the midline at  $2P/4$ , but also the shape of the body has been modified, consequently we observe that the flow pattern is the inverse of the flow pattern found at  $2P/4$ . It is observed that at  $4P/4$ , we have a large counter-clockwise flow structure in the central region, and a small clockwise vortex at the tail. The core of this small vortex is located above the midline of the body. Again we found that the vorticity values and the place where they occur are very similar to those found at  $2P/4$ . In Fig. 10 it is clearly observed that the fish passes a transverse wave along its body. It is also observed that the body undulations generate circular flow patterns that travel along with the body wave. This is in full agreement with experimental data and observations, performed in undulatory natural swimmers [Müller, Smit, Stamhuis, and Videler (2001)]. Further investigation will be carried out by the authors in order to examine the mechanisms by which the body contributes to thrust production in undulatory fish swimming.

Based on the above discussion we will briefly describe our findings for the second case (wave number  $k/2\pi=2$ ). Fig. 11 shows the velocity and vorticity fields at  $P/4$  phases of the tail beat. The period  $P$  and frequency  $\omega$  of the tail beat are now

$P = 10$  s and  $\omega = 0.62$  s<sup>-1</sup> respectively. It is observed that due to the reduction of the amplitude at the tail,  $\hat{h}_1 = 0.03$  m, the size of the large structures is reduced. We also observe that the body undulations generate circular flow patterns that travel along with the body wave. It may be seen that due to the increase of the number of complete waves in the body, the number of vortices has been increased, for instance at  $P/4$  and at  $3P/4$ , it is possible to identify six small vortices, whereas at  $2P/4$  and  $4P/4$ , five vortices are generated. It is observed that the flow pattern at  $P/4$  is the inverse of the flow pattern at  $3P/4$ . The same is observed between the flow patterns at  $2P/4$  and  $4P/4$ . Even though the vortices are smaller than for the first case the vorticity values are of the same order of magnitude. For instance at  $P/4$  ( $3P/4$ ), the maximum value of clockwise (counter-clockwise) vorticity  $\omega_3 = 0.26$  s<sup>-1</sup> ( $\omega_3 = -0.26$  s<sup>-1</sup>) takes place at  $x_1 = 0.68$  m,  $x_2 = 0.51$  m, whereas the maximum value of counter-clockwise (clockwise) vorticity  $\omega_3 = -0.25$  s<sup>-1</sup> ( $\omega_3 = 0.25$  s<sup>-1</sup>) takes place at the tail  $x_1 = 0.83$  m,  $x_2 = 0.49$  m. At  $2P/4$  ( $4P/4$ ) we found that the maximum value of clockwise (counter-clockwise) vorticity  $\omega_3 = 0.17$  s<sup>-1</sup> ( $\omega_3 = -0.17$  s<sup>-1</sup>) takes place at  $x_1 = 0.78$  m,  $x_2 = 0.54$  m, whereas the maximum value of counter-clockwise (clockwise) vorticity  $\omega_3 = -0.25$  s<sup>-1</sup> ( $\omega_3 = 0.25$  s<sup>-1</sup>), takes place at  $x_1 = 0.64$  m,  $x_2 = 0.49$  m. According to the results shown in this section, we may conclude that the MLPG method is a reliable numerical algorithm that can be also used to calculate the flow field induced by the motion of an undulatory body.

#### **7.4 Non-steady flow induced by an elastic body with contraction and expansion movements**

An alternative to undulatory propulsion in water, is propulsion by jet reaction. Animals that possess the jet reaction mode of swimming have the typical "parachute" jellyfish shape. The natural swimmers with medusoid form slowly propel themselves by expelling fluid from their subumbrellar cavity. Existing theoretical models, experimental investigations and numerical computations, have been carried out to describe the kinematics, dynamics and energetics properties of natural swimmers characterized by jet propulsion [Daniel (1983); Ford, Costello, Heidelberg, and Purcell (1997); Sullivan, Suchman, and Costello (1997); Dabiri, Colin, Costello, and Gharib (2005); Sahin and Mohseni (2009)]. Most of the fluid dynamics research work has been focussed to determine the characteristics of the large scale flow structures induced by the fluid efflux that emerge during the subumbrellar cavity contraction (power stroke), and to estimate the vortex formation that occur during the recovery stroke of the propulsive cycle [Dabiri, Colin, Costello, and Gharib (2005)]. Despite the recent contributions aimed to understand the mechanisms that conduct to the efficient propulsion of the medusian animals shape, we

believe that novel numerical methodologies, such as the MLPG method, must be applied to calculate the body-fluid interacting forces (thrust and drag) generated by the vortices surrounding the animal during the power and recovery strokes of the propulsive cycle.

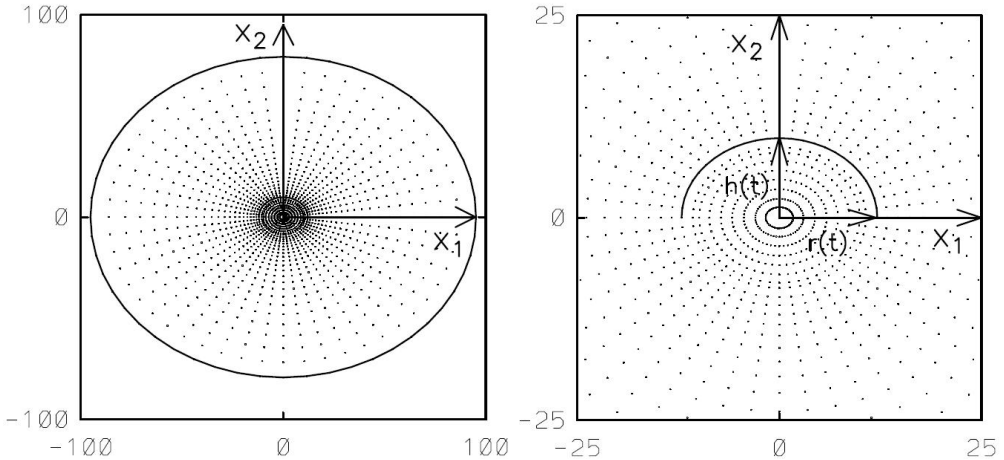


Figure 12: Non-steady flow induced by an elastic body with contraction and expansion movements. Left panel: whole domain with 1560 MLPG nodes. Right panel: closer view of the region surrounding the hemiellipsoidal bell filament.  $r(t)$  is the dimensional radius of the aperture and  $h(t)$  is the dimensional height of the bell.

The system under study is depicted in Fig. 12. Panel on the left shows the whole flow domain, whereas panel on the right shows a closer view of the hemiellipsoidal bell. In order to resolve the viscous flow within the boundary layer in the neighborhood of the jellyfish surface, we increase the number of the MLPG nodes next to the bell. It may be seen that the fluid is confined in a semi-cylindrical cavity, in which a hemiellipsoidal shape elastic filament is immersed. The total number of MLPG nodes used to solve the fluid equations is 1560. The origin of the coordinate system is located at the center of the semi-cylindrical container, and at the center of the two-dimensional hemiellipsoidal bell. Fig. 12 shows the dimensional radius of the aperture  $r(t)$  and the dimensional height  $h(t)$  of the bell. If the radius of the aperture at rest,  $r_r$ , and the velocity,  $r_r\omega$  (where  $\omega = 2\pi/P$  is the frequency of the propulsive periodic movement), are selected as the length scale and the velocity scale of the system respectively, the dimensionless variables for length and velocity may be defined as

$$x_1^* = \frac{x_1}{r_r}, \quad x_2^* = \frac{x_2}{r_r}, \quad v_1^* = \frac{v_1}{r_r \omega}, \quad v_2^* = \frac{v_2}{r_r \omega}. \quad (61)$$

Therefore the dimensionless Navier-Stokes equations can be written as

$$\frac{\partial v_1^*}{\partial x_1^*} + \frac{\partial v_2^*}{\partial x_2^*} = 0, \quad (62)$$

$$\frac{\partial v_1^*}{\partial t^*} + v_1^* \frac{\partial v_1^*}{\partial x_1^*} + v_2^* \frac{\partial v_1^*}{\partial x_2^*} = -\frac{\partial p^*}{\partial x_1^*} + \frac{1}{Re} \nabla^2 v_1^*, \quad (63)$$

and

$$\frac{\partial v_2^*}{\partial t^*} + v_1^* \frac{\partial v_2^*}{\partial x_1^*} + v_2^* \frac{\partial v_2^*}{\partial x_2^*} = -\frac{\partial p^*}{\partial x_2^*} + \frac{1}{Re} \nabla^2 v_2^*, \quad (64)$$

where  $t^* = \omega t$  and  $p^* = p/(\rho r_r^2 \omega^2)$  are the dimensionless time and pressure respectively, and  $Re = r_r^2 \omega / \nu$ , is the Reynolds number. The elastic deformation law of the bell as a function of time is described by three periodic parameters: (i) fineness ratio (bell height  $h(t)$  divided by the bell diameter  $2r(t)$ ), (ii) bell aperture area ( $A(t) = \pi r^2(t)$ ), and (iii) bell volume ( $V(t)$ , whose definition is described below). In order to use the analytical expressions for the kinematics of medusian jet propulsion proposed by Rudolf (2007), which are written in terms of the dimensionless radius of the aperture at rest  $r_r^*$  and the dimensionless volume of the bell at rest  $V_r^*$ , we have defined  $r_r^*$  as

$$r_r^* = (Re)^{1/2} = r_r \left( \frac{\omega}{\nu} \right)^{1/2}. \quad (65)$$

Therefore the aperture radius of the bell as a function of time  $r^*(t^*)$  is defined as [Rudolf (2007)]

$$r^*(t^*) = r_r^* + \gamma \sin^3 t^* + \phi \sin t^*, \quad (66)$$

where  $\gamma$  and  $\phi$  are dimensionless parameters such that  $\gamma + \phi = 1$ . The dimensionless bell volume as a function of time  $V^*(t^*)$  follows the expression

$$V^*(t^*) = V_r^* + \sin(t^* + \varepsilon \sin t^*), \quad (67)$$

where  $\varepsilon$  is a dimensionless parameter controlling the shape of the curve. The selected value of the previous parameters is the following:  $\gamma = 0.3$ ,  $\phi = 0.7$ ,  $r_r^* = 12$

and  $\varepsilon = 2/3$ . The dimensionless height of the bell at rest  $h_r^* = h_r/r_r$  was selected by assuming that the fineness ratio at rest  $f_r = h_r^*/2r_r^* = 0.41$ , therefore  $h_r^* = 10$ . Taking into account both, the radius and the volume at rest ( $r_r^*$  and  $V_r^*$ ), we assume that the bell can be approximated as a hemiellipsoid geometry. If the ellipsoid is a standard axis-aligned body, the radius  $r^*(t^*)$  and the height  $h^*(t^*)$  of the bell correspond to the equatorial radii along the  $x_1^*$  and  $x_2^*$  axis respectively, and the polar radius along the  $x_3^*$  direction is defined as  $c^*(t^*)$ . The volume of a hemiellipsoid  $V^*(t^*)$  as function of time is written as

$$V^*(t^*) = \frac{1}{2} \left( \frac{4}{3} \pi r^*(t^*) h^*(t^*) c^*(t^*) \right) \quad (68)$$

If the polar radius  $c^*(t^*)$  is equal to the radius along the  $x_1^*$  direction,  $r^*(t^*)$ , we have

$$V^*(t^*) = \frac{1}{2} \left( \frac{4}{3} \pi r^*(t^*)^2 h^*(t^*) \right), \quad (69)$$

therefore the volume at rest  $V_r^*$  is calculated as

$$V_r^* = \frac{1}{2} \left( \frac{4}{3} \pi r_r^{*2} h_r^* \right). \quad (70)$$

From Eq. (69) the height  $h^*(t^*)$  as a function of time of the jellyfish is obtained as

$$h^*(t^*) = \frac{3}{2} \frac{V^*(t^*)}{\pi r^*(t^*)^2} \quad (71)$$

Fig. 13 shows the three periodic dimensionless parameters as functions of the dimensionless time  $t^*$ . Panel on the top shows the fineness ratio,  $f(t^*) = h^*(t^*)/2r^*(t^*)$ , the central panel shows the aperture area,  $A(t^*) = \pi r^*(t^*)^2$ , and the bottom panel shows the bell volume,  $V^*(t^*)$ , see Eq. (67). Note that the aperture area (central panel) is divided by the maximum bell area, whereas the bell volume (bottom panel) is normalized between  $\pm 1$  [Rudolf (2007)]. It is also noted that in the three panels, the non-dimensional time is represented by  $t^*/2\pi = t/P$ , where  $P$  is the period of the propulsive cycle.

We have taken into account that the position at rest is located within the recovery stroke, therefore after the end of the power stroke; hence after: (i) the maximum fineness ratio, (ii) minimum aperture area, and (iii) minimum bell volume, see  $t^* = 0$  on the panels of Fig. 13. The Cartesian coordinates of the nodes located on the ellipsoid can be obtained by the following relationships, see Eqs. (66) and (71):

$$x_1^*(t^*) = r^*(t^*) \cos \hat{\beta} \cos \lambda, \quad x_2^*(t^*) = h^*(t^*) \cos \hat{\beta} \sin \lambda. \quad (72)$$

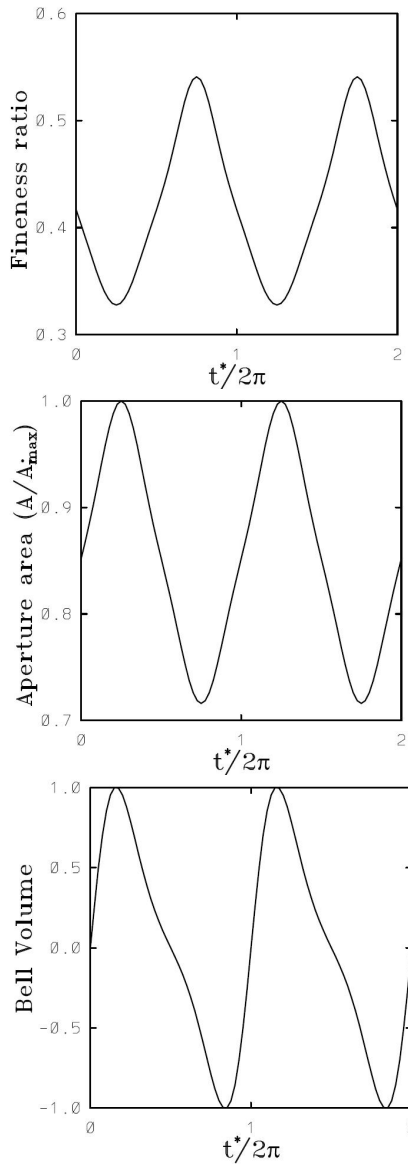


Figure 13: Non-steady flow induced by an elastic body with contraction and expansion movements. Parameters of the elastic deformation law as functions of time. Top panel: fineness ratio. Central panel: aperture area. Bottom panel: bell volume normalized between  $\pm 1$ , [Rudolf (2007)].

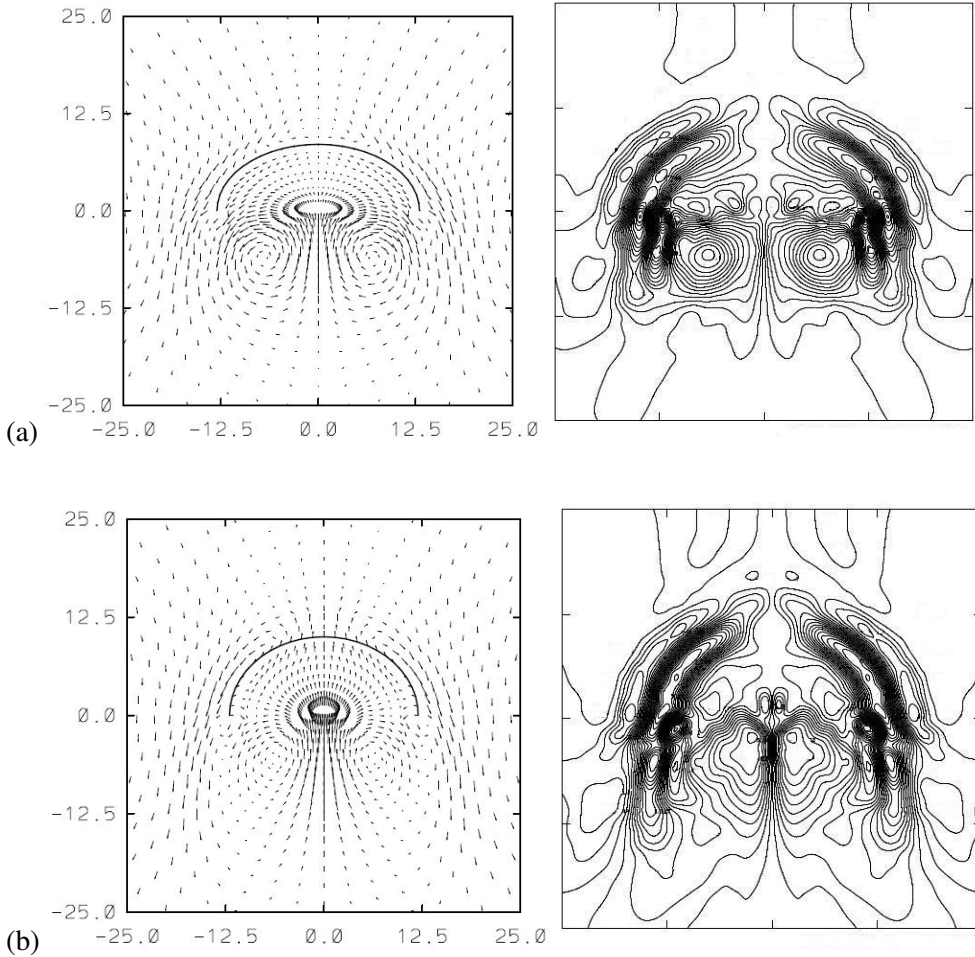


Figure 14: (a) and (b). For caption see next page.

We have assumed the flow as two-dimensional, hence the parametric latitude  $\hat{\beta} = 0$ . Non-slip boundary conditions have been assumed on the semi-cylindrical wall of the container and on the bell. The boundary conditions for the elliptic elastostatic model (displacement vector  $\mathbf{u}$  of the nodes located at the bell) are obtained as it was explained in sections 7.3 and 7.2. The velocity of the nodes at the bell (boundary conditions for the fluid equations) was obtained numerically by dividing the difference of the position vectors at time step  $n + 1$  and at time step  $n$  by the time increment  $\Delta t^*$  i.e.  $\mathbf{v}^* = (\mathbf{x}^{*(n+1)} - \mathbf{x}^{*(n)})/\Delta t^*$ . In the numerical simulations, we fixed the Reynolds number and the dimensionless time increment to  $Re = 144$  and

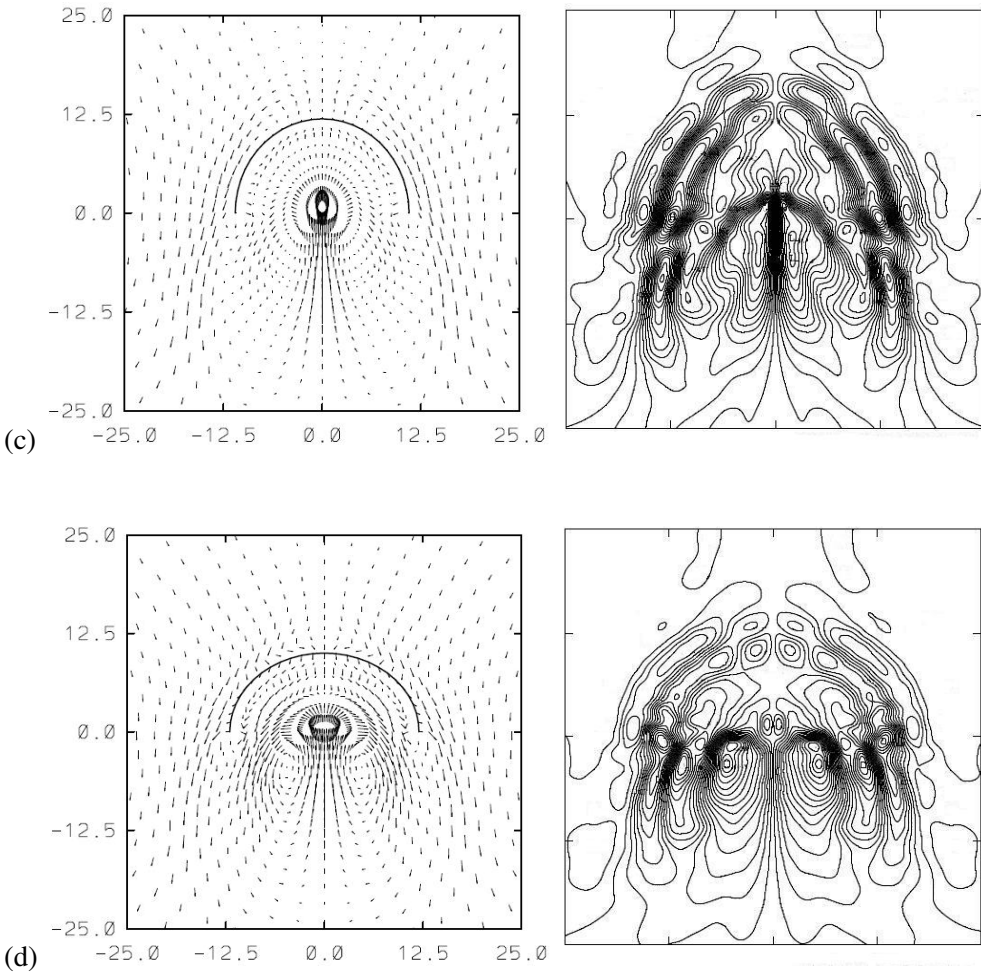


Figure 14: (c) and (d). Non-steady flow induced by an elastic body.  $Re = 144$ . Left column: velocity field. Right column: vorticity field. (a)  $P/4$ , (b)  $2P/4$ , (c)  $3P/4$ , (d)  $4P/4$ .

$\Delta t^* = \Delta t(2\pi/P) = 0.15$ , respectively, We also fixed the period of the propulsive motion to  $P = 1$  s. Fig. 14 shows the velocity and vorticity fields at  $P/4$  phases of the propulsive cycle. It is seen that due to the complex structure of the vorticity field, vortex rings interactions are present during all the phases of the propulsive cycle. At  $P/4$ , end of the recovery stroke, a vortex ring is observed below the bell. The center of the toroidal structure is the symmetry axis. We observe that at  $P/4$

the cavity has been refilled and most of the fluid is not directed by the vortex ring into the bell, but outside the bell by the stream jet formed between the edge of the bell and the core of the vortex ring. However, at the beginning of the recovery stroke, at  $4P/4$ , the volume of the bell begins to increase and the vortex ring below the bell refill the subumbrellar volume (mainly by the stream jet formed around the symmetry axis) with fluid from outside the bell [Dabiri, Colin, Costello, and Gharib (2005)]. As the volume of the bell is reduced  $2P/4$ , the flow pattern is modified and the size of the vortex structures is diminished in the  $x_1$  direction, however along the  $x_2$  direction the size of the flow structures is increased. We observe at  $2P/4$  the formation of vortices at the edges of the bell, it is also observed that flow is being expelled out between the central vortex ring and the vortices at the edges. At the end of the power stroke  $3P/4$ , it is possible to see that the size of the vortices has been increased even more and the internal vortices are not well defined. Notice the small value of the velocities at  $3P/4$ . At  $2P/4$  and  $3P/4$  (contraction of the bell) it is observed that the velocity of the fluid at the upper part of the medusa is increased, this gives at the lower part of the bell an increase on the size of the vortices along  $x_2$  direction. It has been observed by [Sullivan, Suchman, and Costello (1997)] that the velocity of the fluid around the medusa *Aurelia aurita* was greatest during contraction of the bell. They also observed the following: (i) fluid flow around the bell margin transports all species of prey, (ii) prey were carried into the interior of the medusa by the power stroke, (iii) prey captures occurred during power and recovery strokes, implying that during both strokes, fluid flow can be directed into the subumbrellar region. It is important to mention that the phases  $2P/4$  and  $3P/4$  of Fig. 14 resemble figure 2 of the paper by [Sullivan, Suchman, and Costello (1997)]. Our results are also in agreement with the qualitative analysis of the formation and interaction of the vortex rings during the propulsive cycle carried out by [Dabiri, Colin, Costello, and Gharib (2005)]. As they have mentioned during the swim cycle, there is a continuous flow that begins outside the bell, and passes adjacent to the bell margin before entering into the subumbrellar cavity. Fig. 14 shows the continuous flow adjacent to the bell margin and the flow into the subumbrellar cavity. Further research will be conducted by the authors in order to understand the complex relationship between the interaction of vortex ring structures and the resulting non-steady thrust forces governing the swimming of jellyfish. We may conclude that the MLPG method is a reliable methodology that can be used to understand the flow induced by an elastic body with contraction and expansion movements.

## 8 Conclusions

The non-steady, two-dimensional Navier-Stokes equations have been solved by using the MLPG method coupled with a fully implicit pressure correction approach.

The methodology has been validated, through the solution of the flow field induced by a harmonic motion of the bottom lid of a rectangular cavity, and applied to investigate the flow pattern induced by (i) a rigid flapping plate, (ii) an undulatory filament and (iii) an expansion-contraction filament. We have shown that the MLPG method can be used to solve a variety of fluid flow problems in science and engineering where certain surfaces in the flow domain are in arbitrary motion. Such problems frequently appear in nature (natural flyers and swimmers, blood flow in the heart, and blood vessels) and in engineering systems (aerodynamics, hydrodynamics, MEMS, MAV). The preliminary results shown in this paper are in fair agreement with observations available in the literature, and constitute the basis for additional research that will be conducted by the authors aimed to understand the generation of vorticity and the interaction of vortices that produce lift, drag and thrust in natural flyers and swimmers. We may conclude that additional work must be carried out in order to increase the computational performance of the MLPG codes. Particular attention must be focussed on two subjects: (i) parallelize the source codes and (ii) to include a full Arbitrary Lagrangian-Eulerian formulation.

**Acknowledgement:** Financial support for this investigation was provided by DGAPA-UNAM (sabbatical leave of R. Avila at the Center for Aerospace Research & Education, University of California, Irvine) and DGSCA-UNAM through the Visualization Observatory (Ixtli project). Most of the computations were carried out on the supercomputer of DGSCA-UNAM and on the Linux-based 'BDUC' cluster at the University of California, Irvine.

## References

- Atluri, S. N.** (2004): *The Meshless Methods (MLPG) For Domain & Bie Discretizations*. Tech Science Press.
- Atluri, S. N.; Shen, S.** (2002): *The Meshless Local Petrov-Galerkin (MLPG) Method*. Tech Science Press.
- Atluri, S. N.; Shen, S.** (2002): The Meshless Local Petrov-Galerkin (MLPG) method: A simple & less-costly alternative to the Finite Element and Boundary Element methods. *CMES: Computer Modeling in Engineering & Sciences*, vol. 3, pp. 11–51.
- Atluri, S. N.; Zhu, T.** (1998): A new Meshless Local Petrov-Galerkin (MLPG) approach in computational mechanics. *Computational Mechanics*, vol. 22, pp. 117–127.

**Avila, R.; Atluri, S. N.** (2009): The MLPG method for the solution of the heat equation with moving boundaries. *Accepted for publication in the journal: ICCES 'MM8: Advances in the MLPG Method.*

**Avila, R.; Pérez, A.** (2008): A pressure correction approach coupled with the MLPG method for the solution of the Navier-Stokes equations. In M. Griebel and M. A. Schweitzer(Ed): *Lecture Notes in Computational Science and Engineering, Meshfree Methods for partial differential equations IV*, pp. 19–32. Springer.

**Barone, M. F.; Payne, J. L.** (2005): Methods for simulation-based analysis of fluid-structure interaction. Technical Report SAND2005-6573, Sandia National Laboratories, Albuquerque, New Mexico 87185 and Livermore, California 94550, 2005.

**Blackburn, H. M.; Lopez, J. M.** (2003): The onset of three-dimensional standing and modulated travelling waves in a periodically driven cavity flow. *J. Fluid Mech.*, vol. 497, pp. 289–317.

**Carr, L. W.; Chandrasekhara, M. S.** (1996): Compressibility effects on dynamic stall. *Prog. Aerospace Sci.*, vol. 32, pp. 523–573.

**Dabiri, J. O.; Colin, S. P.; Costello, J. H.; Gharib, M.** (2005): Flow patterns generated by oblate medusan jellyfish: field measurements and laboratory analysis. *J. Exp. Biol.*, vol. 208, pp. 1257–1265.

**Daniel, T. L.** (1983): Mechanics and energetics of medusan jet propulsion. *Can. J. Zool.*, vol. 61, pp. 1406–1420.

**Donea, J.; Giuliani, S.; Halleux, J. P.** (1982): An arbitrary Lagrangian-Eulerian finite element method for transient dynamic fluid-structure interactions. *Computer Methods in Applied Mechanics and Engineering*, vol. 33, pp. 689–723.

**Donea, J.; Huerta, A.; Ponthot, J. P.; Rodríguez-Ferran, A.** (2005): Arbitrary Lagrangian-Eulerian methods. In Erwin Stein, René de Borst and Thomas J. R. Hughes(Ed): *Encyclopedia of Computational Mechanics: Vol. 1*. New York: John Wiley.

**Ellington, C. P.** (1984): The aerodynamics of hovering insect flight. II. Morphological parameters. *Phil. Trans. R. Soc. Lond. B.*, vol. 305, pp. 18–40.

**Foias, C.; Manley, O.; Rosa, R.; Temam, R.** (2001): *Navier-Stokes Equations And Turbulence*. Cambridge University Press.

**Ford, M. D.; Costello, J. H.; Heidelberg, K. B.; Purcell, J. E.** (1997): Swimming and feeding by the scyphomedusa *Chrysaora quinquecirrha*. *Mar. Biol.*, vol. 129, pp. 355–362.

**Graham, J. B.; Lowell, W. R.; Rubinoff, I.; Mota, J.** (1987): Surface and subsurface swimming of the sea snake *Pleamislaturus*. *J. Exp. Biol.*, vol. 127, pp. 27–44.

**Gwynllyw, D. R.; Phillips, T. N.** (2005): Some issues regarding spectral element meshes for moving journal bearing systems. *Int. J. Numer. Meth. Fluids*, vol. 48, pp. 423–454.

**Ho, S.; Nassef, H.; Pornsinsirirak, N.; Tai, Y. C.** (2003): Unsteady aerodynamics and flow control for flapping wing flyers. *Progress in Aerospace Sciences*, vol. 39, pp. 635–681.

**Hughes, T.; Liu, W. K.; Zimmermann, T. K.** (1981): Lagrangian-Eulerian finite element formulation for incompressible viscous flows. *Computer Methods in Applied Mechanics and Engineering*, vol. 29, pp. 329–349.

**Karniadakis, G. E.; Sherwin, S. J.** (1999): *Spectral/hp Element Methods for CFD*. Oxford University Press.

**Lighthill, M. J.** (1960): Note on the swimming of slender fish. *J. Fluid Mechanics*, vol. 9, pp. 305–317.

**Lighthill, M. J.** (1969): Hydromechanics of aquatic animal propulsion. *Annu. Rev. Fluid Mech.*, vol. 1, pp. 413–446.

**Lighthill, M. J.** (1970): Aquatic animal propulsion of high hydromechanical efficiency. *J. Fluid Mechanics*, vol. 44, pp. 265–301.

**Lin, H.; Atluri, S. N.** (2000): Meshless Local Petrov Galerkin (MLPG) method for convection-diffusion problems. *CMES: Computer Modeling in Engineering & Sciences*, vol. 1, pp. 45–60.

**Lin, H.; Atluri, S. N.** (2001): The Meshless Local Petrov-Galerkin (MLPG) method for solving incompressible Navier-Stokes equations. *CMES: Computer Modeling in Engineering & Sciences*, vol. 2, pp. 117–142.

**Martinelli, R. C.; Boelter, L. M. K.** (1938): The effect of vibration on heat transfer by free convection from a horizontal cylinder. In *Proceedings of 5th International Congress of Applied Mechanics*, pp. 578–586.

**Müller, U. K.; Smit, J.; Stamhuis, E. J.; Videler, J. J.** (2001): How the body contributes to the wake in undulatory fish swimming: Flow fields of a swimming eel (*Anguilla Anguilla*). *J. Exp. Biol.*, vol. 204, pp. 2751–2762.

**Pedley, T. J.; Hill, S. J.** (1999): Large-amplitude undulatory fish swimming: fluid mechanics coupled to internal mechanics. *The Journal of Experimental Biology*, vol. 202, pp. 3431–3438.

**Rønquist, E. M.** (1988): *Optimal Spectral Element Methods for the unsteady three-dimensional incompressible Navier-Stokes equations*. Phd Thesis, Massachusetts Institute of Technology.

**Rudolf, D.** (2007): *Animating Jellyfish through numerical simulation and symmetry exploitation*. Msc. Thesis, University of Saskatchewan, Saskatoon.

**Sahin, M.; Mohseni, K.** (2009): An arbitrary Lagrangian-Eulerian formulation for the numerical simulation of flow patterns generated by the hydromedusa *Aequorea victoria*. *Journal of Computational Physics*, vol. 228, pp. 4588–4605.

**Shyy, W.; Berg, M.; Ljungqvist, D.** (1999): Flapping ad flexible wings for biological and micro air vehicles. *Prog. Aerospace Sci.*, vol. 35, pp. 455–505.

**Stein, K.; Tezduyar, T.; Benney, R.** (2003): Mesh moving techniques for fluid-structure interactions with large displacements. *Journal of Applied Mechanics*, vol. 70, pp. 58–63.

**Sullivan, B. K.; Suchman, C. L.; Costello, J. H.** (1997): Mechanics of prey selection by ephyrae of the scyphomedusa *Aurelia aurita*. *Marine Biology*, vol. 130, pp. 213–222.

**Vogel, M. J.; Hirs, A. H.; Lopez, J. M.** (2003): Spatio-temporal dynamics of a periodically driven cavity flow. *J. Fluid Mech*, vol. 478, pp. 197–226.